Galactic accretion and the outer structure of galaxies in the CDM model

Andrew P. Cooper[1,2⋆], Richard D'Souza[1], Guinevere Kauffmann[1], Jing Wang[1], Michael Boylan-Kolchin[3], Qi Guo[2,4], Carlos S. Frenk[4] and Simon D.M. White[1]

[1] *Max-Planck-Institut für Astrophysik, Karl-Schwarzschild-Str. 1, D-85748, Garching, Germany*
[2] *National Astronomical Observatories, Chinese Academy of Sciences, 20A Datun Road, Chaoyang, Beijing 100012, China*
[3] *Center for Cosmology, Department of Physics and Astronomy, 4129 Reines Hall, University of California, Irvine, CA 92697, USA*
[4] *Institute for Computational Cosmology, Department of Physics, University of Durham, South Road, Durham, DH1 3LE, UK*

ABSTRACT

We have combined the semi-analytic galaxy formation model of Guo et al. (2011) with the particle-tagging technique of Cooper et al. (2010) to predict galaxy surface brightness profiles in a representative sample of ~ 1900 massive dark matter haloes (10^{12}–10^{14} $M_{\odot}$) from the Millennium II ΛCDM N-body simulation. Here we present our method and basic results focusing on the outer regions of galaxies, consisting of stars accreted in mergers. These simulations cover scales from the stellar haloes of Milky Way-like galaxies to the 'cD envelopes' of groups and clusters, and resolve low surface brightness substructure such as tidal streams. We find that the surface density of accreted stellar mass around the central galaxies of dark matter haloes is well described by a Sèrsic profile, the radial scale and amplitude of which vary systematically with halo mass (M_{200}). The total stellar mass surface density profile breaks at the radius where accreted stars start to dominate over stars formed in the galaxy itself. This break disappears with increasing M_{200} because accreted stars contribute more of the total mass of galaxies, and is less distinct when the same galaxies are averaged in bins of stellar mass, because of scatter in the relation between $M_{\star}$ and M_{200}. To test our model we have derived average stellar mass surface density profiles for massive galaxies at $z \approx 0.08$ by stacking SDSS images. Our model agrees well with these stacked profiles and with other data from the literature and makes predictions that can be more rigorously tested by future surveys that extend the analysis of the outer structure of galaxies to fainter isophotes. We conclude that it is likely that the outer structure of the spheroidal components of galaxies is largely determined by collisionless merging during their hierarchical assembly.

Key words: galaxies: structure; galaxies: elliptical and lenticular, cD; galaxies: bulges; galaxies: evolution

1 INTRODUCTION

Hierarchical clustering leads to the coalescence of dark matter haloes. Galaxies are formed 'in situ' by the cooling and condensation of gas in the cores of these haloes (White & Rees 1978) and accrete additional stars from the debris of their hierarchical progenitors. The aim of this paper is to predict how the surface density profiles of galaxies reflect changes in the balance between in situ star formation and stellar accretion during their hierarchical growth over the lifetime of the universe.

The idea of using observations of accreted stars to test theories of galaxy evolution has its roots in the study of the stellar halo and globular clusters of the Milky Way and M31 (Baade 1944; Eggen,

Lynden-Bell & Sandage 1962; Searle & Zinn 1978). The recent discovery of cold stellar streams in these haloes, some with identifiable progenitors, has provided direct evidence that they grow at least partly through the tidal disruption of companion galaxies (e.g. Ibata, Gilmore & Irwin 1995; Belokurov et al. 2006; Niederste-Ostholt et al. 2010; McConnachie et al. 2009). Stellar haloes and streams appear to be a generic feature of late-type galaxies (Zibetti, White & Brinkmann 2004; Richardson et al. 2009; Martínez-Delgado et al. 2010a; Bailin et al. 2011; Radburn-Smith et al. 2011). Shell-like structures have been detected around both early and late type galaxies (Malin & Carter 1983; Schweizer 1980; Schweizer et al. 1990; Schweizer & Seitzer 1992; Tal et al. 2009; Martínez-Delgado et al. 2010a) and can also be readily explained as the result of galactic accretion in a cold dark matter (CDM) universe (e.g Cooper et al. 2011). Galaxies at the centres of mas-

sive clusters are often surrounded by extended envelopes of diffuse 'intracluster light' (ICL) (Matthews, Morgan & Schmidt 1964; Oemler 1976; Thuan & Romanishin 1981; Schombert 1988; Graham et al. 1996; Lin & Mohr 2004; Gonzalez, Zabludoff, & Zaritsky 2005; Mihos et al. 2005; Krick, Bernstein, & Pimbblet 2006; Donzelli, Muriel, & Madrid 2011) which is also thought to originate from the stripping and disruption of satellite galaxies (Gallagher & Ostriker 1972).

Semi-analytic models of galaxy formation aim to quantify the importance of the accretion of stars and gas in different types of galaxy (White & Frenk 1991; Cole 1991; Kauffmann, White & Guiderdoni 1993; Somerville & Primack 1999; Cole et al. 2000; Baugh et al. 2005; De Lucia & Blaizot 2007; Benson & Bower 2010; Guo et al. 2011). In particular, they predict how the mass of stars accreted by a galaxy depends on the mass and assembly time of its dark matter halo, as well as the number of progenitors of the halo and their individual star formation histories. Such models predict that only the most massive galaxies at the present day are dominated by stars accreted in mergers; in galaxies less massive than the Milky Way, most stars form in situ from gas cooling directly from their halo (Baugh, Cole & Frenk 1996; Kauffmann 1996; De Lucia et al. 2006; Naab et al. 2007; Purcell, Bullock, & Zentner 2007; Guo & White 2008; Parry, Eke, & Frenk 2009).

Accretion and merger events may still affect the colour, size and morphology of a galaxy even if they make a limited contribution to its mass. They are therefore thought to be relevant to the dichotomy between early and late-type morphologies in the Hubble sequence (e.g. Toomre 1977; Fall 1979; Frenk et al. 1985; Cowie et al. 1994; Zepf 1997; Kauffmann & Charlot 1998; Cole et al. 2000; Bell et al. 2004; Sales et al. 2012) and many well-known scaling relations between observable properties of massive galaxies (Faber & Jackson 1976; Kormendy 1977; Djorgovski & Davis 1987; Peletier et al. 1990; Bender, Burstein & Faber 1992; Kauffmann et al. 2003b; Bernardi et al. 2003), including correlations between the luminosity of massive elliptical galaxies and the amplitude and shape of their projected surface brightness profiles (Kormendy 1977; Binggeli, Sandage & Tarenghi 1984; Schombert 1986; Graham & Guzmán 2003; Kormendy et al. 2009; Graham 2011, and references therein).

The effects of stellar accretion on galactic structure depend on the population of infalling galaxies and the rate at which haloes coalesce as well as the gravitational dynamics of the accretion process. This means that galactic accretion cannot be studied in isolation from galaxy formation. The way in which accreted stars are deposited in the outer regions of galaxies and the consequent change in observables such as half-light radius and stellar mass has been considered extensively in recent literature (Daddi et al. 2005; Trujillo et al. 2006; van Dokkum et al. 2010). Simulations focussing on this issue by e.g. Naab, Khochfar & Burkert (2006); Naab et al. (2007); Naab, Johansson, & Ostriker (2009) and Oser et al. (2010) have highlighted the importance of N-body dynamical simulations when making quantitative predictions for the evolution of galaxy sizes and velocity dispersions in CDM (compare González et al. 2009; Guo et al. 2011; Shankar et al. 2013). Notably, these simulations suggest that high mass ratio mergers contribute significantly to the structure of massive elliptical galaxies (Hilz et al. 2012; Hilz, Naab & Ostriker 2013).

In this paper we use an extension of the Guo et al. (2011, hereafter G11) semi-analytic galaxy formation model to predict the spatial distribution of all stars accreted on to present-day massive galaxies. Like many recent numerical studies of the size evolution of massive quiescent galaxies (Meza et al. 2003; Naab et al. 2009;

Oser et al. 2010) and Milky Way-like galaxies (Abadi, Navarro & Steinmetz 2006; Cooper et al. 2010; Font et al. 2011; Sales et al. 2012) we emphasize the difference between in situ star formation and galactic accretion in our analysis. The semi-analytic component of our model provides the full in situ star formation histories of galaxies and all their hierarchical progenitors, matching constraints such as the galaxy stellar mass function. In addition, we use an N-body method to predict how each accreted population evolves in all six dimensions of phase space. Our model is applied to the Millennium II simulation, which contain ~ 2000 haloes in the mass range $10^{12} < M_{200} < 10^{14}\,\mathrm{M_\odot}$. We can therefore make a statistical comparison to observational data on the total amount of accreted light around galaxies and its distribution. In this paper, we only consider galaxies at the centres of virialised dark haloes at $z = 0$, although our model can also make predictions for galaxies at high redshift and for galaxies that are satellites at the present day. We focus on the spatial distribution of accreted stars, but we note that our model also predicts their kinematic properties and chemical abundances.

A statistical study of this sort is motivated by the availability of moderately deep wide-field imaging from surveys such as SDSS Stripe 82 and PanSTARRS, which will enable us to determine the extent to which results obtained from the Milky Way and M31 stellar haloes are applicable to the galaxy population as a whole. Previous studies of galaxy structure in large surveys have focused on regions of high surface brightness (e.g. Shen et al. 2003), because the outskirts of galaxies are usually much fainter than the sky, even in the case of the envelopes around brightest cluster galaxies (BCGs). Stacking (e.g. Zibetti et al. 2005; Tal & van Dokkum 2011) is a promising technique for studying the average properties of these regions. We have therefore carried out our own stacking analysis using imaging data from SDSS, for comparison to our models.

We proceed as follows. In Section 2 we describe how we select a sample of massive central galaxies from the Millennium II simulation. We also summarize how our particle-tagging method works. Section 3 shows examples of the stellar haloes of individual galaxies in our model. In Section 4 we present our main statistical results in the form of average stellar mass surface density profiles for haloes and galaxies of different mass, highlighting differences between in situ and accreted stars. We compare with observations from the literature in Section 5 and from our own stacking analysis in Section 6. Section 7 interprets trends in surface brightness profile shape by studying the origin of accreted stars in our simulation. We summarise our findings in Section 8. Appendix A discusses the numerical convergence of our method and differences with our previous work on particle tagging. Appendix B describes the technical details of our SDSS stacking analysis.

2 SIMULATIONS

2.1 Semi-analytic model

Millennium II (Boylan-Kolchin et al. 2009) is a collisionless N-body simulation of ΛCDM structure formation in a comoving volume of $10^6\,h^{-3}\,\mathrm{Mpc^3}$ with a flat ΛCDM cosmology, $\Omega_\mathrm{m} = 0.25$, $\Omega_\Lambda = 0.75$ and Hubble parameter $h = 0.73$. The particle mass is $6.89 \times 10^6\,h^{-1}\,\mathrm{M_\odot}$. The semi-analytic galaxy model of G11 is based on halo merger trees derived from Millennium II and its parameters are tuned to fit the SDSS stellar mass function of Li & White (2009; grey dashed line in Fig. 1). Figure 7 of G11 shows that when same model is applied to the Millennium Simulation
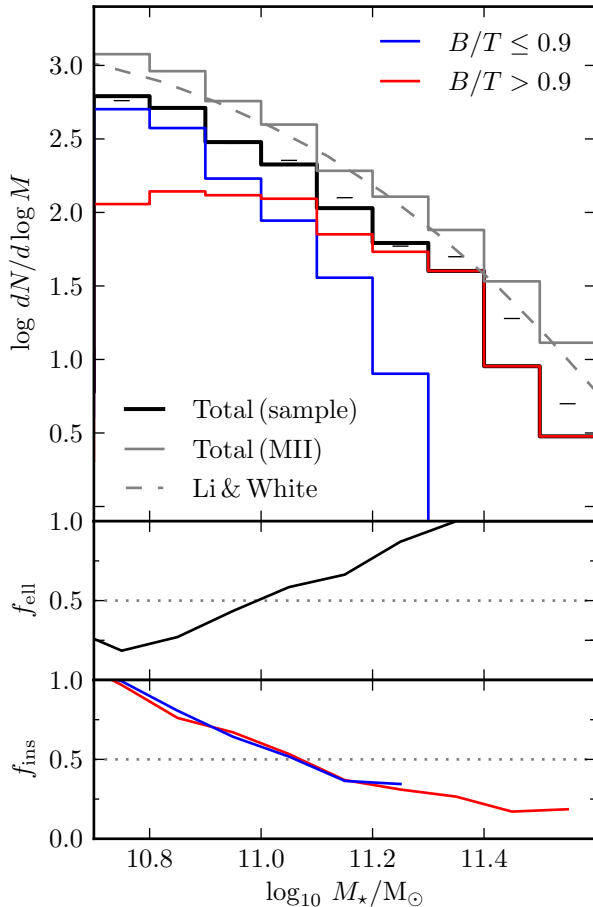
Figure 1. The solid black histogram shows the mass function of our primary sample of central galaxies from the G11 model. The solid grey histogram is the mass function of *all* galaxies in the Millennium II simulation, including satellite galaxies and all galaxies associated with the merger tree of the most massive cluster which we have excluded from our analysis. The dashed grey line shows the Li & White (2009) SDSS mass function normalized to the Millennium II volume, derived as in Appendix A of Guo et al. (2010) and assuming the same Chabrier IMF as our model. Red and blue histograms split the mass function of our primary sample into two components based on bulge-to-total mass ratio, as shown in the legend. Short black horizontal lines (between the black and grey histograms) show the effect of including the G11 prediction of diffuse stellar halo mass for each galaxy in our sample. Considering only our sample galaxies, the lower two panels show (top) the fraction, $f_{\rm ell}$, of galaxies in each mass bin with $B/T > 0.9$, and (bottom) the fraction of the combined bulge and disc stellar mass in each bin that was formed in situ, split by B/T as in the main panel.

(Springel et al. 2005), which has a larger volume, it overpredicts the number of galaxies with $\log_{10} M_\star/M_\odot \gtrsim 11.5$. G11 suggest that this discrepancy is due to sample variance and $\sim 1\,{\rm mag}$ luminosity uncertainties for the most luminous galaxies in SDSS (see e.g. Bernardi et al. 2013).

From the results of G11 we select 1872 *central* galaxies more massive than $M_\star = 5 \times 10^{10}\,{\rm M_\odot}$ at $z = 0$. The stellar mass function of these galaxies is shown by the black histogram in Fig. 1. We do not select all the galaxies in the simulation above our threshold stellar mass (in particular, we exclude satellite galaxies and the central galaxy of the most massive cluster). The grey histogram shows the mass function of all galaxies in the simulation to demonstrate that this selection does not bias our sample.

The G11 model uses a combination of two 1D axisymmetric density profiles to represent the distribution of stars inside galaxies (an exponential disc and a Jaffe-model bulge[1]) and quantifies galaxy morphology using the ratio of bulge mass to total stellar mass, B/T. The red histogram in Fig. 1 shows the mass function of galaxies with $B/T \geqslant 0.9$ ('ellipticals') and the blue histogram the mass function of galaxies with $B/T < 0.9$. We plot the ratio of these mass functions in the middle panel. The fraction of 'elliptical' galaxies increases from 50 to 100 per cent in the interval $11.0 < \log_{10} M_\star/M_\odot < 11.3$. This is in good agreement with observations (e.g. Conselice 2006, see figure 4 of G11) and a similar transition scale has been found in other semi-analytic models (De Lucia et al. 2011). These models also predict differences between early and late-type K-band luminosity functions that are qualitatively similar to those observed (Benson & Devereux 2010).

We define 'in situ' stars as those that are still gravitationally bound to the dark matter halo in which they formed. G11 predict that more massive galaxies form less of their total stellar mass in situ. The lowest panel of Fig. 1 shows that the fraction of stars in each mass bin formed in situ decreases from almost (but of course not exactly) 100 per cent at $\log_{10} M_\star/M_\odot = 10.7$ to 50 per cent at $\log_{10} M_\star/M_\odot = 11.1$. The mass fraction of in situ stars in systems with $B/T \geqslant 0.9$ is similar to that of other galaxies regardless of stellar mass. This implies that in the G11 model, the relative contribution of in situ star formation depends primarily on stellar mass and not morphology[2]. For the most massive galaxies plotted Fig. 1, the fraction of stars formed in situ is ~ 19 per cent. Thus the model makes a clear prediction that accreted stellar populations will dominate the structure of the most massive galaxies.

2.2 Particle tagging

We use a technique we call particle tagging to predict the stellar population mix and spatial distribution of stars in galaxies, based on the merger trees and star formation histories of the G11 model. This technique uses additional information from the underlying N-body simulation in order to predict more observables than standard semi-analytic models, without running a new simulation. Other studies using particle tagging techniques include Bullock, Kravtsov & Weinberg (2001), Napolitano et al. (2003), Bullock & Johnston (2005), Peñarrubia, Navarro & McConnachie (2008) and Laporte et al. (2013), although these were not coupled to the predictions of semi-analytic models. We give a brief summary of our method below; for more detail see Cooper et al. (2010, hereafter C10). A discussion of minor differences between our implementation and that of C10 and a test of convergence with their results can be found in Appendix A.

The particle tagging technique associates ('tags') sets of dark matter particles in an N-body simulation (here Millennium II) with

---

[1] G11 also track the total mass in a diffuse stellar halo component but do not specify its density profile. The mass in this component is only a significant fraction of the total galaxy stellar mass above $\log_{10} M_\star/M_\odot \sim 11.2$. Horizontal bars in Fig. 1 show how including the G11 stellar halo component in the central galaxy stellar mass affects the stellar mass function of our sample at $z = 0$.

[2] Since galaxies with $B/T > 0.9$ were formed by low mass ratio mergers, one might expect their in situ fractions to be lower than those of galaxies with the same mass having $B/T < 0.9$. However, in the G11 model, merger-induced starbursts and disc instabilities can increase the in situ mass while also increasing B/T.

stellar populations of a single metallicity and age. The tagged particles can be used to track the evolution of their associated population in phase space, from the time when the stars form to the present day ($z = 0$). Our definition of a stellar population comprises all the stars formed in a single galaxy between two consecutive snapshots of the G11 model. An isolated galaxy that forms stars at a constant rate for a Hubble time will produce a number of these populations equal to the number of simulation snapshots. All model galaxies at $z = 0$ are a superposition of many such populations, because they accrete populations formed in their hierarchical progenitors as well as forming their own stars in situ.

For every population, particles are selected according to a tagging criterion (described below). An equal fraction of the total mass of the population is given to each particle thus selected. Every new population tags a new set of particles, selected from the corresponding dark matter halo at the snapshot immediately after the population forms. This means that a DM particle can be tagged more than once, if it meets the tagging criterion for two or more populations (by construction, this can only happen at different snapshots). In such cases, each tag is tracked separately. A corollary is that each tagged particle carries its own unique star formation and enrichment history, with the time resolution of the Millennium II snapshots.

2.3   Tagging criterion and the $f_{\rm mb}$ parameter

The particles we select for tagging are supposed to approximate the phase space distribution of the stars immediately after they form. Stars are the end result of dissipative collapse, so a basic requirement is that particles tagged with newly-formed stars should be deeply embedded in the potential well of their dark halo when we tag them. We achieve this by ranking DM particles in the halo by their binding energy and selecting all those more bound than a threshold value, corresponding to a fixed fraction of the mass of the halo. Following C10, we call this free parameter of the method the 'most-bound fraction', $f_{\rm mb}$. A value of $f_{\rm mb} = 0.01$ means we selected the 1 per cent most-bound particles.

The choice of $f_{\rm mb}$ is more-or-less arbitrary, but this freedom allows us to tune the scale length of the in situ components of our galaxies in a predictable way. This is because, in an NFW potential (Navarro, Frenk & White 1996), the surface density profile of dark matter more bound than a given energy is roughly exponential (at least for $f_{\rm mb} < 10$ per cent), with a scale radius that depends on the threshold energy. This result can be verified easily by integrating the cumulative energy distribution of an NFW halo up to a given fraction of its virial mass, and constructing the corresponding density profile from the phase space distribution function. We have done this using numerical approximations for the distribution function and density of states given by Widrow (2000) for a spherical NFW halo with an isotropic velocity distribution.

To illustrate this point, Fig. 2 shows the profile of in situ stars in two 'Milky Way' mass haloes from Millennium II (top and bottom panels), according to our full particle tagging model (dots) with $f_{\rm mb} = 1\%$ (blue) and $f_{\rm mb} = 10\%$ (red). Dotted lines show the profile we obtain using the Widrow (2000) distribution function to select the equivalent most-bound mass fraction at $z = 1$, by which time most of the stars in these galaxies have already formed (the central regions of these haloes are very stable thereafter, e.g. Wang et al. 2011). The dotted profiles are not exactly exponential because our procedure obviously imposes an energy threshold, which corresponds to a truncation radius. Solid lines show exponential profiles that have the same scale radius as the dotted profiles – these roughly
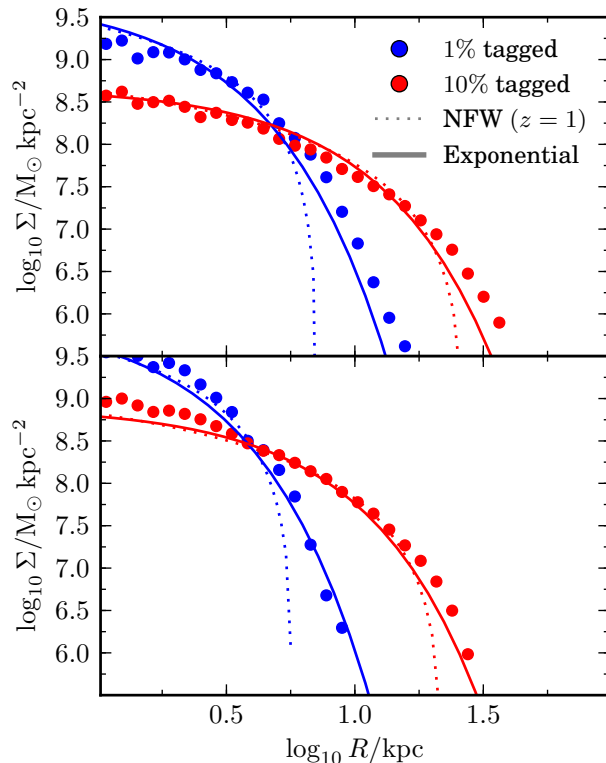

Figure 2. Dots show in situ surface density profiles in two Milky Way-like haloes at $z = 0$ from G11, predicted by our particle tagging model with $f_{\rm mb} = 1\%$ (blue) and 10% (red). Upper and lower panels respectively correspond to galaxies with $M_{200} = (12.1, 12.3)$, $M_\star = (10.8, 10.9)$ and NFW concentration $c = (7.2, 8.2)$. Dotted lines show density profiles for the corresponding fractions of most bound DM particles at $z = 1$ (assuming an isotropic NFW distribution function with virial radius and concentration given by the N-body halo of each galaxy), normalized to the same stellar mass. Solid lines show exponential profiles with the same amplitude and half mass radius as the dotted lines.

approximate the diffusion of tagged particles across the initial energy threshold over time. Note that because we perform our tagging procedure at every snapshot, each new population in our full model will have a different amount of time to diffuse away from its initial configuration.

We stress that our model for the structure of merger remnants is not purely collisionless, because the G11 model explicitly includes enhanced dissipative star formation (in the bulge component) during mergers. This is important because hydrodynamical simulations of galaxy mergers have shown that nuclear starbursts increase the central phase space density of merger remnants (Hernquist, Spergel & Heyl 1993; Robertson et al. 2006; Hopkins et al. 2008). We include stars formed in these bursts in our tagging in the same way as those formed in the 'quiescent' mode.

2.4   Constraints on $f_{\rm mb}$ from the galaxy mass–size relation

From the above we conclude that our analytic approximation can reproduce the $z = 0$ density profiles of particles that we tag to represent in situ stars with reasonable accuracy. This provides an intuitive understanding of why the parameter $f_{\rm mb}$ sets the sizes of galaxies dominated by in situ star formation, and how those sizes vary with the scale of the dark matter potential. Based on this,
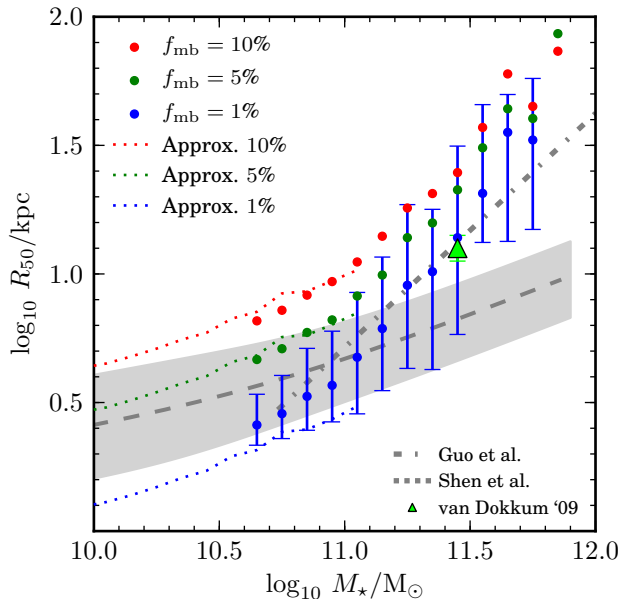
Figure 3. Points plot stellar mass $M_\star$ against projected half-mass radius R_{50} for all galaxies in our full particle tagging models; colours correspond to different values of f_{mb}. Dotted lines of the same colours show our analytic approximation for the sizes of all central galaxies in Millennium II, using their in situ stellar mass and $z = 1$ halo properties. The dashed grey line and shaded region plot the late-type galaxy relation of Shen et al. (2003) and its 1σ range. The dot-dashed grey line shows the early-type galaxy relation of Guo et al. (2009) corrected from a Kroupa to a Chabrier IMF using $\Delta \log_{10} M_\star/M_\odot = -0.04$. The green triangle corresponds to a stack of deep images of 14 nearby ellipticals (van Dokkum et al. 2010).

we can determine a range of suitable f_{mb} values empirically, by comparing the predicted relation between stellar mass ($M_\star$) and projected half-mass radius (R_{50}) to observations of galaxies dominated by in situ star formation, i.e. those with $\log_{10} M_\star \lesssim 10.8$; e.g. Guo & White 2008). By using only in situ stars to constrain f_{mb}, the distribution of accreted stars remains a valid prediction of our model. With a similar approach, C10 found that $f_{mb} = 1\%$ gave reasonable agreement between their simulations and the $M_\star$–R_{50} relation of dwarf satellite galaxies in the Local Group. We re-examine the choice of f_{mb} because C10 considered only galaxies that were predominantly satellites, with very different stellar and dark matter mass scales to those in our simulation.

In Fig. 3 we show the median $M_\star$–R_{50} relation for all galaxies in our full particle tagging model at $z = 0$ (red, green and blue points, corresponding to $f_{mb} = 10\%, 5\%$ and 1% respectively). Each galaxy in the model contributes three values of R_{50} from three orthogonal projections to its $M_\star$ bin. Model galaxies have a considerable scatter in R_{50} at fixed stellar mass (the 16–84 percentile range for $f_{mb} = 1$ per cent is shown by the error bars on the blue points; other values of f_{mb} have very similar scatter). Note that our sample contains only 13 galaxies with $M_\star > 10^{11.5} M_\odot$.

At $M_\star \lesssim 10^{11} M_\odot$, where galaxies in our model are dominated by in situ stars, we can use our analytic approximation to extrapolate our results below the limit of $M_\star \geqslant 5 \times 10^{10} M_\odot$ we imposed when selecting galaxy merger trees for tagging. We take all central galaxies at $z = 0$ in the G11 Millennium II catalogue with $10^8 \leqslant M_\star < 10^{11.1} M_\odot$ and use the virial radius (r_{200}) and

concentration[3] c of their dark matter haloes at $z = 1$ to predict R_{50} at $z = 0$. These predictions are shown as dotted lines in Fig. 3. They agree roughly with the results of the full tagging model in the range where they overlap, although we find that R_{50} is underestimated by $\sim 33\%$ for $f_{mb} = 1\%$. This is not surprising as the $f_{mb} = 1\%$ results are most sensitive to the simple representation of the central dark matter potential.

This extrapolation confirms that our tagging model produces a curved $\log_{10} M_\star$–$\log_{10} R_{50}$ relation similar to the observed relation of Shen et al. (2003) for late-type galaxies (grey dashed line with 1σ scatter). At lower $M_\star$ the model with $f_{mb} = 1\%$ underpredicts the observed relation. Our approximation predicts that a model with $f_{mb} \approx 3\%$ would be closer to the data; $f_{mb} = 5\%$ is also plausible, as the Shen et al. (2003) relation may underpredict the sizes of edge-on galaxies by ~ 0.15 dex (e.g. Dutton et al. 2007). On the other hand, the relation from our model also includes early-type galaxies, which are known to be significantly more compact at than late-types at $M_\star \lesssim 10^{11} M_\odot$ (Shen et al. 2003). Kauffmann et al. (2003a) do not separate galaxies by morphology and find $R_{50} = 2.38$ kpc ($h = 0.73$) for $10.0 < \log_{10} M_\star < 10.5$ which supports $1\% \lesssim f_{mb} \lesssim 3\%$.

Having determined a plausible range of f_{mb} with reference to in situ stars, we can now examine the predictions of these models for more massive galaxies that are dominated by accreted stars. In Fig. 3, the mass–size relation clearly steepens at $M_\star > 10^{11} M_\odot$ (e.g. Shen et al. 2003; Hyde & Bernardi 2009). In this regime the $f_{mb} = 1\%$ model follows approximately the relation for early-type galaxies found by Guo et al. (2009; grey dot-dashed line[4]). This relation agrees with the results of van Dokkum et al. (2010) (green triangle), who stacked Sérsic fits to individual deep images of 14 galaxies with $\log_{10}\langle M_\star\rangle/M_\odot = 11.45$ from a mass-selected and approximately volume-limited sample of early types (Tal et al. 2009).

A value of $f_{mb} = 5\%$, which gives a reasonable scale for in situ stars in lower-mass galaxies, overpredicts R_{50} from Guo et al. (2009) by ~ 0.15 dex at $M_\star > 10^{11} M_\odot$. A value of $f_{mb} = 10\%$ overpredicts R_{50} by $\lesssim 0.3$ dex, indicating that our predictions for R_{50} in this mass range are less sensitive to f_{mb} than they are for in-situ dominated galaxies, where R_{50} changes by ~ 0.5 dex over the same range in f_{mb}. As we will show in the following section, this sensitivity is still mostly driven by the strong effect of f_{mb} on the scale of in situ stars even in very massive galaxies. The effects on the accreted component are even weaker, the most notable being an increase in R_{50} with f_{mb} because more extended satellite galaxies are more easily stripped.

The apparent excess in R_{50} at $M_\star > 10^{11.5} M_\odot$ even for an $f_{mb} \sim 1\%$ model may arise in part because masses and sizes derived from SDSS photometric measurements miss a substantial fraction of light in the outer regions of massive galaxies with high Sérsic index (Graham et al. 2005; Bernardi et al. 2007; Lauer et al. 2007; Blanton et al. 2011; Bernardi et al. 2012; Meert et al. 2012; Mosleh, Williams & Franx 2013).

Subject to this uncertainty, we conclude that the median half-mass radii of accretion-dominated galaxies in our models are consistent with observations for $1\% < f_{mb} \lesssim 3\%$. We prefer not to

---

[3] We determine c as $c = 2.16 \, r_{200}/r_{max}$ where r_{max} is the radius of maximum circular velocity (e.g Cole & Lacey 1996).

[4] We note that the observations plotted in figure 8 of Guo et al. (2009) for $M_\star > 10^{11.5} M_\odot$ lie systematically above the linear relation we plot, which suggests that the relation may curve upwards at higher $M_\star$ (e.g. Bernardi et al. 2011).

fine-tune a 'best' choice of f_{mb}. Effects including the treatment of in situ star formation in G11, the cosmology of Millennium II and the accuracy of observed $M_\star$ and R_{50} values (e.g. Bernardi et al. 2013, Mitchell et al. 2013 and references therein) may determine how well our tagging model matches the observations, because 1% changes in f_{mb} correspond to 0.1 dex differences in R_{50} and $M_\star$. Therefore, in order to bracket the plausible range of f_{mb} and to show how it affects our conclusions, we will use fiducial values of $f_{\mathrm{mb}} = 1\%, 5\%$ and 10% for the remainder of the paper.

2.5   Limitations of the method

The most important limitation of particle tagging is that it neglects the gravitational effects of concentrating baryons in the cores of dark matter haloes. C10 considered only the highly dark matter dominated dwarf satellites of Milky Way-like galaxies. Here, however, we tag dark matter particles in galaxies of Milky Way mass and larger, where the gravitational potential within R_{50} could be modified significantly by baryons (e.g. Koopmans et al. 2009). If this effect was included in our model, our central galaxies may be more concentrated and the cores of our satellites more robust to tidal stripping. These effects may explain the ~ 0.1 dex overestimate of R_{50} at $M_\star \gtrsim 10^{11} M_\odot$ in Fig. 3 (for an $f_{\mathrm{mb}} \sim 3\%$ model). Another limitation is that a tagging method based on binding energy alone cannot model rotationally supported discs, thus even 'late type' galaxies are represented by dispersion-supported spheroidal systems[5]. Finally, we neglect the possibility that in situ stars form on very loosely bound orbits far away from galaxies, for example from cold gas clumps stripped from satellites or ejected in galactic fountains.

The first two limitations mean that, in the N-body part of our model, we cannot include the formation and secular evolution of discs, adiabatic contraction or the destruction of cusps in dark haloes by feedback (Navarro, Eke & Frenk 1996; Gnedin et al. 2004; Dutton et al. 2007; Pontzen & Governato 2012). As discussed in the previous section, the stellar mass surface density profiles of late-type galaxies in our model are exponential, and their scale lengths can be roughly matched to observations by choosing f_{mb} appropriately. Nevertheless, the energy and angular momentum distribution of stars in disc galaxies may affect the details of their stripping and disruption (e.g. Chang, Macciò & Kang 2013). Satellites in our model do not suffer tidal shocking or enhanced (stellar) dynamical friction from the stars of their central galaxy, which may artificially favour their survival. On the other hand, both limited numerical resolution and the absence of gravitational binding energy from stars will artificially enhance the rate of satellite disruption.

We proceed with these approximations nevertheless as a first step towards modelling the spatial distribution and other properties of the diffuse stellar component of galaxies, in the context of a realistic model of galaxy formation. Our model for in situ stars is only intended to serve as a means of creating initial conditions for accretion events with roughly the right scale and concentration, and as a means of quantifying the relative contribution of accreted stars at different radii.

3   RESULTS FOR INDIVIDUAL GALAXIES

Before we present surface density profiles of galaxies averaged in bins of stellar mass and halo mass, we illustrate the basic output of our model with 12 examples of individual galaxies from our sample of 1872.

3.1   Images

Fig. 4 shows 2D images of projected stellar mass surface density for twelve of our simulated galaxies ($f_{\mathrm{mb}} = 1\%$). The stellar mass associated with each tagged dark matter particle has been smoothed over a cubic spline kernel with a scale radius enclosing its 64 nearest dark matter neighbours (e.g. Springel 2005). Satellite galaxies (tagged particles in self-bound subhalos) have been removed, so the remaining 'lumps' on small scales are due to shot noise in the particle distribution.

The galaxies labelled A–D in Fig. 4 represent the lowest halo masses in our sample, with $M_{200} \approx 10^{12}\,\mathrm{M_\odot}$ and $M_\star \approx 6 \times 10^{10}\,\mathrm{M_\odot}$ (similar to the Milky Way, e.g. Li & White 2008; McMillan 2011). Those labelled E–H are more massive isolated haloes with $M_{200} \approx 10^{12.5}\,\mathrm{M_\odot}$ and slightly larger $M_\star$, while those labelled I–L represent the central galaxies of groups and poor clusters, with $10^{13.25} < M_{200} < 10^{14}\,\mathrm{M_\odot}$ and $M_\star$ up to $2 \times 10^{11}\,\mathrm{M_\odot}$. The G11 model predicts that B, C, D, G and K have $B/T < 0.2$, and J has $B/T \sim 0.4$. The other examples fall into our 'early type' category defined by $B/T > 0.9$.

The colour scale for surface mass density illustrates the observability of different features. Regions with red colours are readily observable in the Sloan Digital Sky Survey; $\mu_r < 25\,\mathrm{mag\,arcsec^{-2}}$) whereas those with yellow/green colours require deep imaging ($25 < \mu_V < 28\,\mathrm{mag\,arcsec^{-2}}$, e.g. Martínez-Delgado et al. 2010b). Careful reduction of SDSS images (in particular those in Stripe 82) can achieve $26 < \mu_r < 28\,\mathrm{mag\,arcsec^{-2}}$ (e.g. Kaviraj 2010; Bakos & Trujillo 2012) and the next generation of imaging surveys will reach these depths routinely (LSST Science Collaborations et al. 2009). Regions with $\mu_r \sim 31\,\mathrm{mag\,arcsec^{-2}}$ (blue colours) are currently only accessible with resolved starcounts in nearby galaxies (e.g. Bland-Hawthorn et al. 2005; Barker et al. 2009; Bailin et al. 2011; Radburn-Smith et al. 2011) and through stacking enembles of similar galaxies (Zibetti et al. 2004, 2005; Tal & van Dokkum 2011).

3.2   Individual density profiles

The solid lines in Fig. 5 show the stellar mass surface density profiles of the 12 galaxies from Fig. 4. Galaxies in the three panels (representing different ranges of M_{200} and $M_\star$) show clear differences in the shape of their profiles, as well as the expected differences in amplitude between galaxies of different mass. Whereas there are no clear differences in the appearance of the galaxies in the first two columns of Fig. 4, the late type galaxies (B, C, D and G) clearly show two structural components in Fig. 5: an exponentially-declining inner profile that breaks to a shallower slope at radii between 10 kpc and 30 kpc. This break is not seen in the profiles of their early type counterparts (A, E, F, H), which have roughly constant slope from 5 kpc to 100 kpc[6].

---

[5] We can still separate galaxies by morphology using the G11 B/T ratio, which is independent of our tagging approach.

[6] The shape of the profile and the classification of the galaxy as early or late type in the G11 model are not directly connected; they are only correlated by the dependence of both on the mass accretion history.
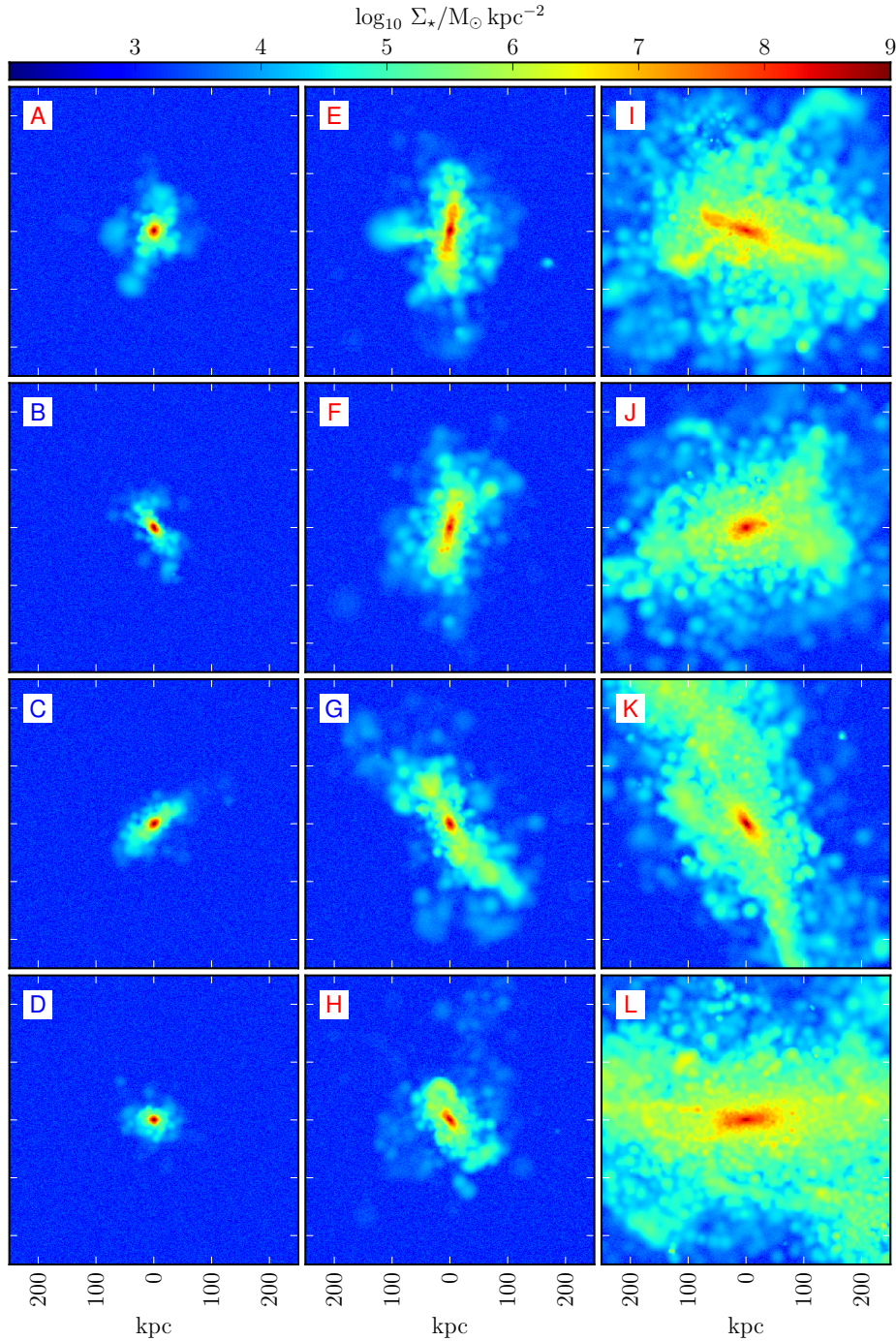
Figure 4. Projected stellar mass surface density in regions 500×500 kpc around 12 simulated galaxies. In each of the three columns, M_{200} and $M_\star$ are approximately constant, representing (from left to right) Milky Way-like galaxies, massive isolated galaxies, and group/cluster central galaxies. These examples are referred to in the text by their labels A–L (blue where G11 $B/T \leqslant 0.9$ and red where G11 $B/T > 0.9$). More details are shown in Fig. 5. Satellite galaxies are included in the model but are not shown for clarity. $\Sigma = 7.0\,(6.0, 5.0)\,\mathrm{M_\odot\,kpc^{-2}}$ corresponds to a V band surface brightness of $\sim 24.8\,(27.3, 29.8)\,\mathrm{mag\,arcsec^{-2}}$ assuming a mass-to-light ratio of 2.5 (see Fig. 5 for this approximate conversion scale). We have imposed a minimum surface density of $\Sigma = 3.0\,\mathrm{M_\odot\,kpc^{-2}}$ ($\sim 35\,\mathrm{mag\,arcsec^{-2}}$) with Poisson noise to create the 'background' in these images. The lumpy appearance of the diffuse light is due to shot noise in the adaptively smoothed particle distribution.
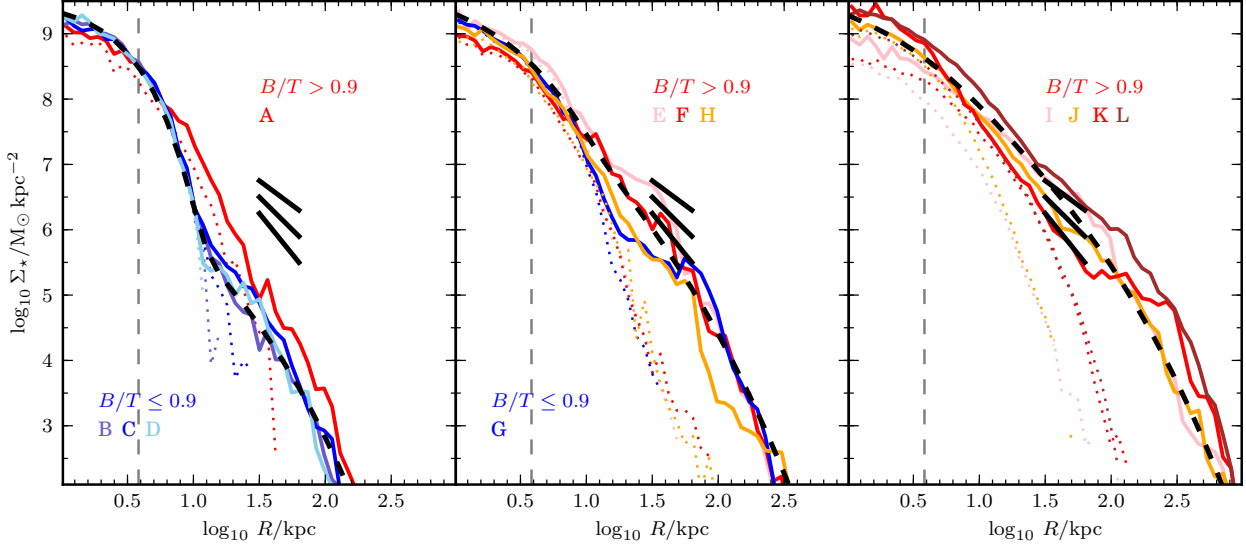
Figure 5. Solid lines show stellar mass surface density profiles for the galaxies shown in Fig. 4 (identified by letters A–L). Line colours correspond to G11 B/T values as shown in the legend. Short black solid lines show slopes of -1.5, -2.0 and -2.5 for reference. The thick dashed black lines are the average total density profiles for galaxies with the same halo mass as the examples, discussed in section 4. Dotted lines show the density of in situ stars only. A vertical dashed line marks the effective force softening scale.

The inner regions of these galaxies (< 10 kpc) are very similar to each other, even for different halo masses and at radii well outside the effective force softening scale (shown by a vertical dashed line[7]). Coloured dotted lines in Fig. 5 show that in situ stars dominate these regions. Although the in situ component grows in size with halo mass, the mass of the accreted component that dominates at larger radii increases even more rapidly. The surface density at ~ 100 kpc, which is almost entirely contributed by accreted stars in all our examples, increases by three orders of magnitude across the panels.

Therefore, the physical origin of the break mentioned above is the transition from regions dominated by in situ stars to regions dominated by accreted stars. This implies a clear connection between the typical shapes of galaxy surface brightness profiles and the relative fraction and distribution of accreted stars. The rest of this paper will focus on the importance of accreted stars in changing the surface brightness profile shape as a function of halo mass, using all the galaxies in our sample.

4   AVERAGE SURFACE DENSITY PROFILES

Figure 6 shows the main results of this paper: the median profiles of stellar mass surface density in circular annuli, for all the galaxies in our sample in logarithmic bins of 0.5 dex in dark halo virial mass (M_{200}). In this figure we only show results for $f_{mb} = 1\%$, for clarity. We do not take projections along the principal axes of the galaxies or align them in any other way, so the relative orientations of the profiles we combine are random.

The profiles of total stellar mass surface density (blue lines) show a tight correlation in shape and amplitude with M_{200}, with 80 per cent of profiles differing by no more than 0.5 dex from the

median at all radii in all halo mass bins (a large part of this scatter, shown by the light blue band, is due to the 0.5 dex width of our halo mass bins). The separate contributions of accreted and in situ stars explain the shape of the profiles and their variation with halo mass. In situ stars (red dotted lines) dominate the high surface brightness regions in haloes up to $\sim 10^{13} M_\odot$, while accreted stars (red dashed lines) dominate at radii greater than 30 kpc and in more massive haloes. Regardless of M_{200}, neither the two subcomponents nor the combined stellar profile follow the NFW distribution of the dark matter (purple lines).

Fig. 7 shows examples of Sèrsic (1968) functions (c.f. Graham & Driver 2005) fit to our median in situ and accreted surface density profiles. We find that both components are well described by such fits across the entire M_{200} range of our sample and for $1\% < f_{mb} < 10\%$. By construction, the total profile is best fit by the sum of these two functions – a single Sèrsic function is only an appropriate model for the *total* surface density in haloes more massive than $M_{200} \sim 10^{13} M_\odot$, where the accreted component dominates at all radii. Even in these haloes, the in situ component makes a significant contribution, and a slight change in shape due to the transition between accreted and in situ stars is still apparent at $R < 10$ kpc.

Fig. 8 repeats Fig. 6 but bins galaxies by stellar mass, $M_\star$, rather than M_{200}. The strong trends with M_{200} are less clear in the case of $M_\star$, except in the most massive stellar mass bin. The cause of this is the considerable scatter in the $M_\star$–M_{200} relation (e.g. Guo et al. 2010). Below their half-mass radii, the median surface brightness profiles are hard to distinguish across a range of $10.7 < \log_{10} M_\star < 11.2$. A stronger variation of the profiles with $M_\star$ can be seen at larger radii, ~ 30–100 kpc.

Fig. 8 also illustrates the effects of varying f_{mb}, over the range 1–10 per cent. Relative to the 1 per cent profiles (blue lines), the 10 per cent profiles (red lines) are ~ 30 per cent more extended and have lower central surface density (see section 2.3). This rescaling of the in situ component is the main effect of changing f_{mb}. The most significant impact of higher f_{mb} on the accreted component

---

[7] Forces are exactly Newtonian for particle separations greater than $2.8\epsilon = 3.84$ kpc with $h = 0.73$ and Plummer-equivalent softening length $\epsilon = 1 h^{-1}$kpc fixed in comoving coordinates.
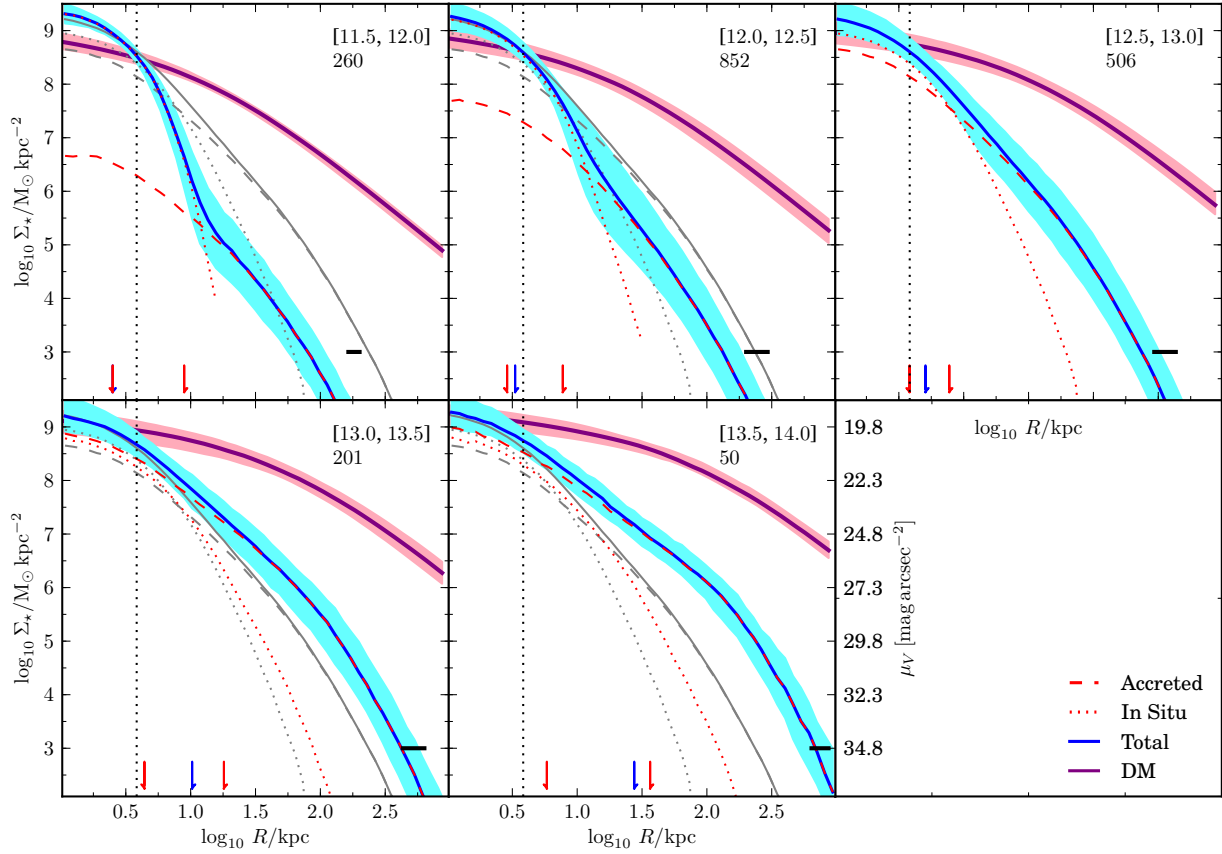
Figure 6. Median profiles of circularly averaged stellar mass surface density, $\Sigma_\star$, for accreted stars (red dashed lines) and in situ stars (red dotted lines), in logarithmic bins of dark halo virial mass (range of $\log_{10} M_{200}/M_\odot$ and number of galaxies per bin are shown in the top right of each panel). A blue solid line shows the median profile for $f_{mb} = 1\%$ combining accreted and in situ components; a light blue region indicates the 10–90 per cent scatter of the median profile. Arrows indicate half-mass radii of the median profiles (from left to right, in situ stars, all stars and accreted stars). Grey lines (dotted, dashed and solid) reproduce the corresponding red and blue lines from the $12.5 < \log_{10} M_{200}/M_\odot < 13.0$ panel. A purple line and pink shading show the median dark matter density profile and its 10–90 per cent range. A black horizontal bar shows the range of R_{200} in each mass bin, and a vertical dotted black line indicates the effective softening scale 2.8ϵ. The scale on the right of the lower central panel gives an approximate conversion from $\Sigma_\star$ to surface brightness (in Vega magnitudes per square arcsecond) for the Johnson-Cousins V band, assuming $\Upsilon_V = M_\star/L_V = 2.5$.
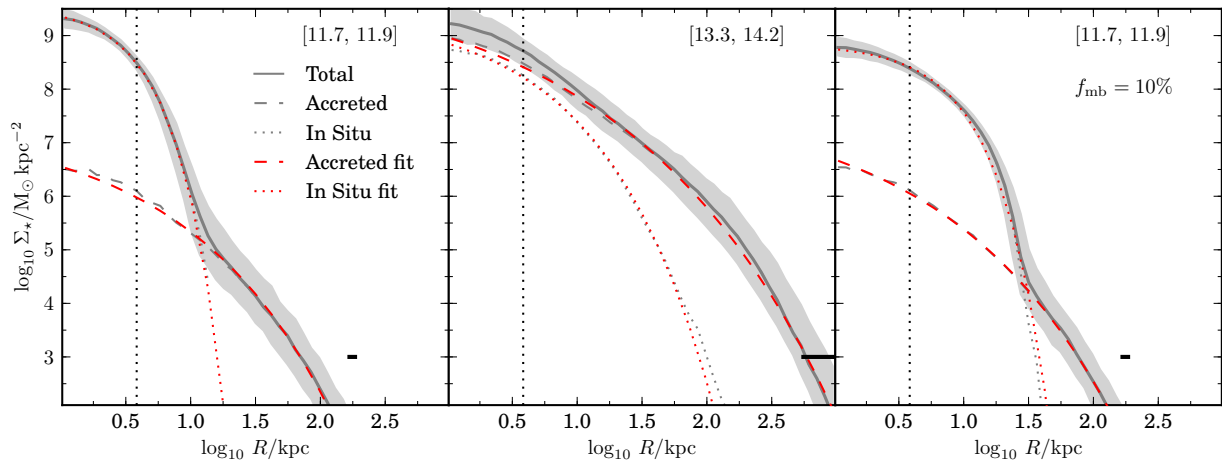

Figure 7. Average stellar mass surface density profiles as in Fig. 6 for our 100 least massive haloes (left) and 100 most massive haloes (centre) with $f_{mb} = 1\%$, and our 100 least massive haloes with $f_{mb} = 10\%$ (right). Legends indicate the corresponding range of $\log_{10} M_{200}/M_\odot$. Grey lines show our simulation results, red lines show Sérsic model fits to the accreted (dashed) and in situ (dotted) components, which overplot the simulation data almost everywhere. From left to right, the Sérsic parameters of the accreted star fits are $[\log_{10} \Sigma_{50}/M_\odot \, kpc^{-2}, R_{50}/kpc, n] = [5.31, 10.4, 2.56], [7.21, 24.6, 3.64]$ and $[5.37, 10.1, 2.96]$. The in situ star fits are $[9.00, 2.3, 0.79], [7.96, 5.5, 1.90]$ and $[8.21, 5.4, 0.88]$.
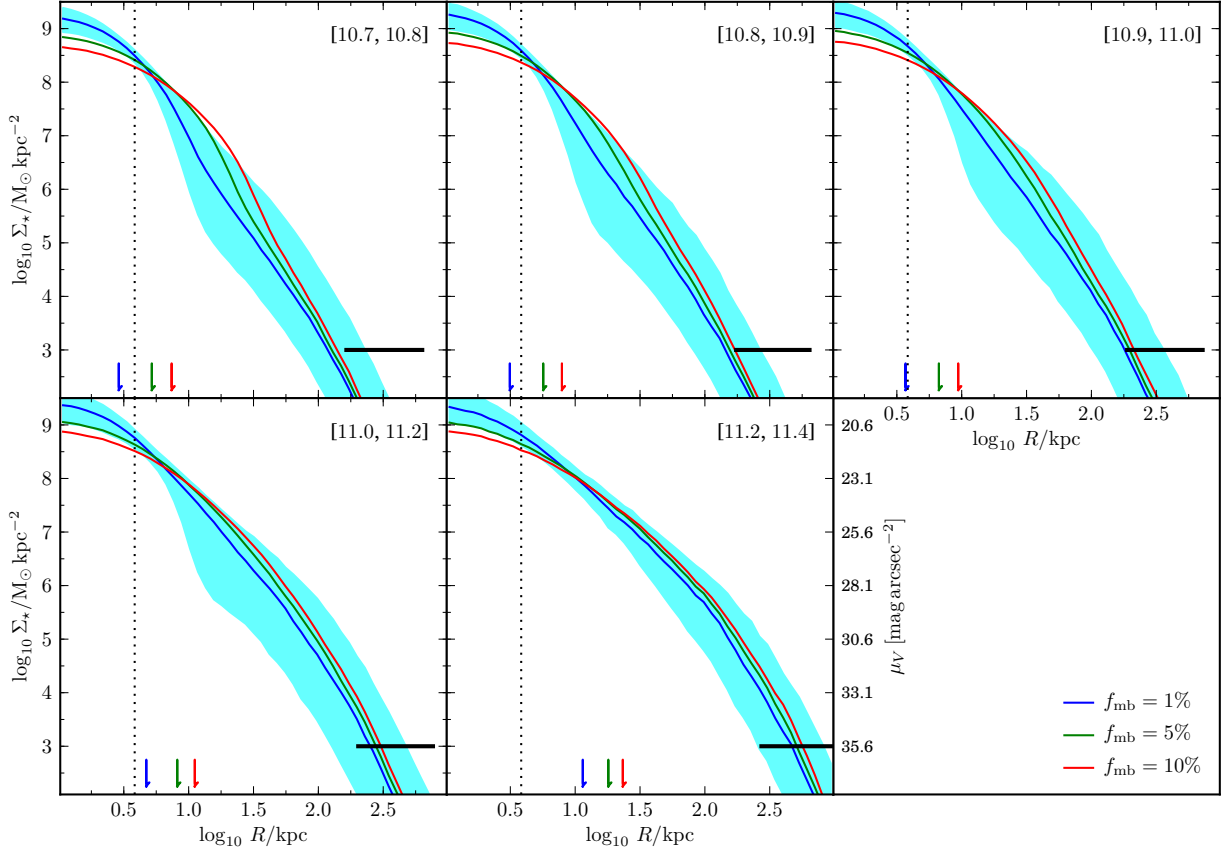
Figure 8. Surface density profiles in bins of total stellar mass, $M_\star$. Note that the final two bins are wider than the first three. Different line colours correspond to different choices of $f_{\rm mb}$, which mainly affect the in situ component; the effect on the accreted component is negligible except in the most massive galaxies (see Appendix A). The light blue region indicates the 10–90 per cent scatter of the median profile for the $f_{\rm mb} = 1\%$ case. Arrows show half mass radii and black lines show the range of R_{200} in each bin.
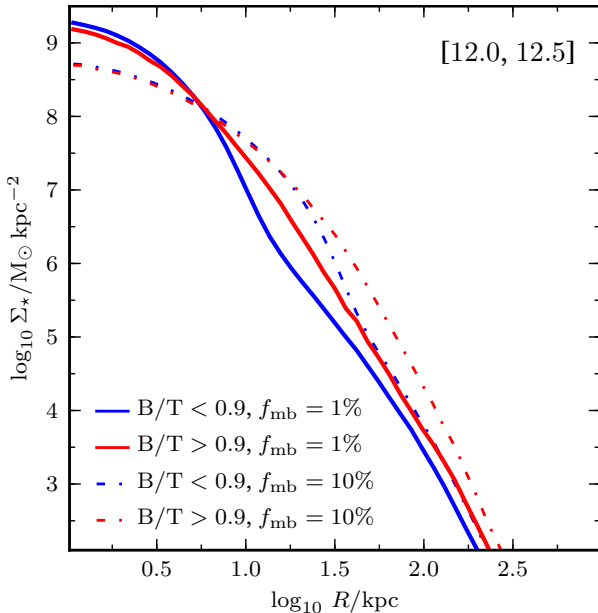
Figure 9. Average stellar mass surface density profiles for $f_{\rm mb} = 1\%$ (solid lines) and 10% (dot-dashed lines) in the halo mass bin $12.0 < \log_{10} M_{200} < 12.5$, subdivided into galaxies with $B/T < 0.9$ ($N = 704$, blue lines) and with $B/T > 0.9$ ($N = 132$, red lines).

is in the very outer regions of the most massive galaxies, where slightly more stars are found on weakly bound orbits (perhaps as the result of earlier stripping). Again we conclude that our density profile results do not depend strongly on the value of $f_{\rm mb}$, at least within a range consistent with the observed mass–size relation.

In Section 3.2 we discussed an interesting relationship between the bulge-to-total stellar mass ratio B/T (predicted by the G11 model) and the shape of the surface density profiles we obtain with particle tagging. In Figure 9 we show that this result holds on average, plotting the $f_{\rm mb} = 1\%$ profile in the bin $12.0 < \log_{10} M_{200} < 12.5$ (top-centre panel of Figure 6) separately for galaxies with $B/T > 0.9$ and $B/T < 0.9$. The latter profile shows a clear inflection at ~ 10 kpc, which corresponds to the radius at which accreted stars begin to dominate over in situ stars. The absence of this break in galaxies with $B/T > 0.9$ reflects a greater contribution of accreted stars to the inner parts of galaxies and the action of violent relaxation in major mergers (the primary cause of high B/T in the G11 model), which makes the profiles of the two components more similar. Figure 9 shows that profiles of galaxies with low and high G11 B/T can still be distinguished if we use a much higher value of $f_{\rm mb}$, although the accreted-in situ break is then much less clear. We caution that the value of B/T is calculated in a simple manner and is influenced by other processes in the G11 model (such as disc instabilities and starbursts). In individual cases it does not correspond perfectly to a separation between
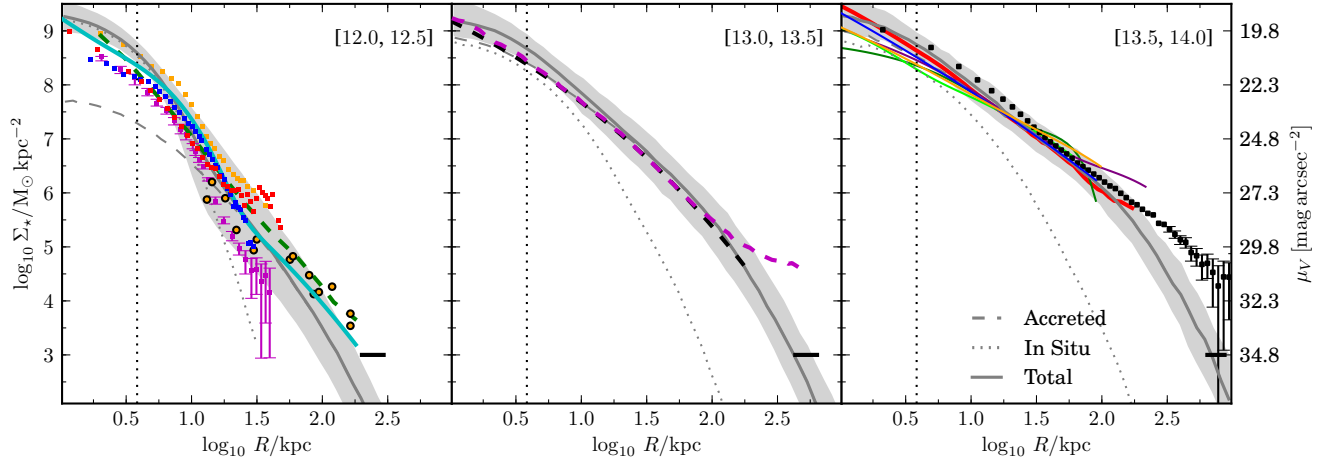
Figure 10. As Fig. 6. The surface density profiles in each bin of halo mass for $f_{\mathrm{mb}} = 1\%$ only are shown in grey, and compared with observational data (and other simulations) given in Table 1. The assignment of galaxies to halo mass bins for the observational data is approximate.

Table 1. Surface mass density profile data shown in Fig. 10. From left to right, columns give: the range of halo mass to which the data (or simulations) are compared ($\log_{10} M_{200}/\mathrm{M}_\odot$, corresponding to panels in Fig. 10); the target galaxy or galaxies; the source of the data; the symbol or line style used in Fig. 10; the photometric bandpass of the data; the stellar mass-to-light ratio we have assumed (where the original authors do not present their results in terms of stellar mass surface density); and comments on the data (LTG: late type galaxy).

Halo mass	Galaxies	Reference	Marker	Band	$M_\star/L$	Comments
[12.0, 12.5]	M81	Barker et al. (2009)	Orange squares	V	2.5	LTG
	M31	Gilbert et al. (2009)	Orange circles	V	2.5	LTG
	M31	Courteau et al. (2011)	Cyan line	I	1.5	LTG, composite profile from various sources
	NGC 1087	Bakos & Trujillo (2012)	Blue squares	$ugriz$	–	LTG, $\Sigma_\star$ from authors
	NGC 7716	Bakos & Trujillo (2012)	Red squares	$ugriz$	–	LTG, $\Sigma_\star$ from authors
	NGC 2403	Barker et al. (2012)	Magenta squares	V	2.5	LTG
	GIMIC	Font et al. (2011)	Green dashes	V	2.5	Stack of ~ 400 simulated LTGs
[13.0, 13.5]	LRG stack	Tal & van Dokkum (2011)	Magenta line	r	2.0	Stack, $N = 42579$, $\langle z \rangle \sim 0.34$
	OBEY sample	van Dokkum et al. (2010)	Black line	r	2.0	Sèrsic profile fit to stacked Tal et al. (2009) data
[13.5, 14.0]	NGC 6173	Seigar, Graham & Jerjen (2007)	Blue line	R	2.0	BCG, Abell 2197
	UGC 9799	Seigar et al. (2007)	Dark green line	R	2.0	BCG, Abell 2052
	NGC 3551	Seigar et al. (2007)	Orange line	R	2.0	BCG, Abell 1177
	GIN 478	Seigar et al. (2007)	Purple line	R	2.0	BCG, Abell 2148
	NGC 4874	Seigar et al. (2007)	Light green line	R	2.0	BCG, Coma cluster
	M87	Kormendy et al. (2009)	Red line	V	2.5	BCG, Virgo cluster
	BCG stack	Zibetti et al. (2005)	Black squares	i	1.5	Stack of SDSS MaxBCG clusters, richness > 15

two-component and quasi-power-law profiles in our tagged particle model.

5 COMPARISON WITH LITERATURE DATA

In Fig. 10 we compare the surface density profiles shown in Fig. 6 (binned by M_{200}) with deep observational data from a variety of sources (summarised in Table 1). We do this to illustrate the variety of different surface density profiles that have been reported in the literature, rather than to match any particular observation. In most cases our choice of an M_{200} bin for each observational dataset is based on the observed stellar mass (e.g. Guo et al. 2010; Moster et al. 2010) and is thus very rough. Where authors have presented their data in terms of stellar mass surface density, we use their values directly. Otherwise, since we find that all but our lowest-mass simulated galaxies have very shallow $M_\star/L$ gradients at $R > 10$ kpc, we assume a galaxy-wide $M_\star/L$ appropriate to each bandpass (listed in Table 1, based on the ages and metallic-

ities of our simulated stars and the models of Bruzual & Charlot 2003 with a Chabrier 2003 IMF). There are many systematic differences between these datasets (including photometric bandpass, surface brightness dimming corrections, K-corrections, cosmology and in some cases, the choice of IMF). We have attempted to correct for these differences where necessary. Such corrections amount to less than 0.1 dex in most cases.

In the halo mass range $12.0 < \log_{10} M_{200}/\mathrm{M}_\odot < 12.5$ we show data from galaxies comparable to the Milky Way and M31 ($M_{200} \sim 10^{12}\mathrm{M}_\odot$, e.g. Watkins et al. 2010). The composite I band profile of M31 from Courteau et al. (2011, cyan line) agrees well with the average profile of accreted stars in our model (dashed grey line) for $R \lesssim 50$ kpc. At $R > 100$ kpc Courteau et al. find a higher surface density than our model; this portion of their profile is based on the individual fields of Gilbert et al. (2009; orange dots), some of which may contain substructure. The galaxies M81 (Barker et al. 2009), NGC 2403 ($M_\star \sim 10^{10}\mathrm{M}_\odot$; Barker et al. 2012), NGC 1087 ($M_\star \sim 10^{10.4}\mathrm{M}_\odot$) and NGC 7716 ($M_\star \sim 10^{10.5}M_\odot$; Bakos &
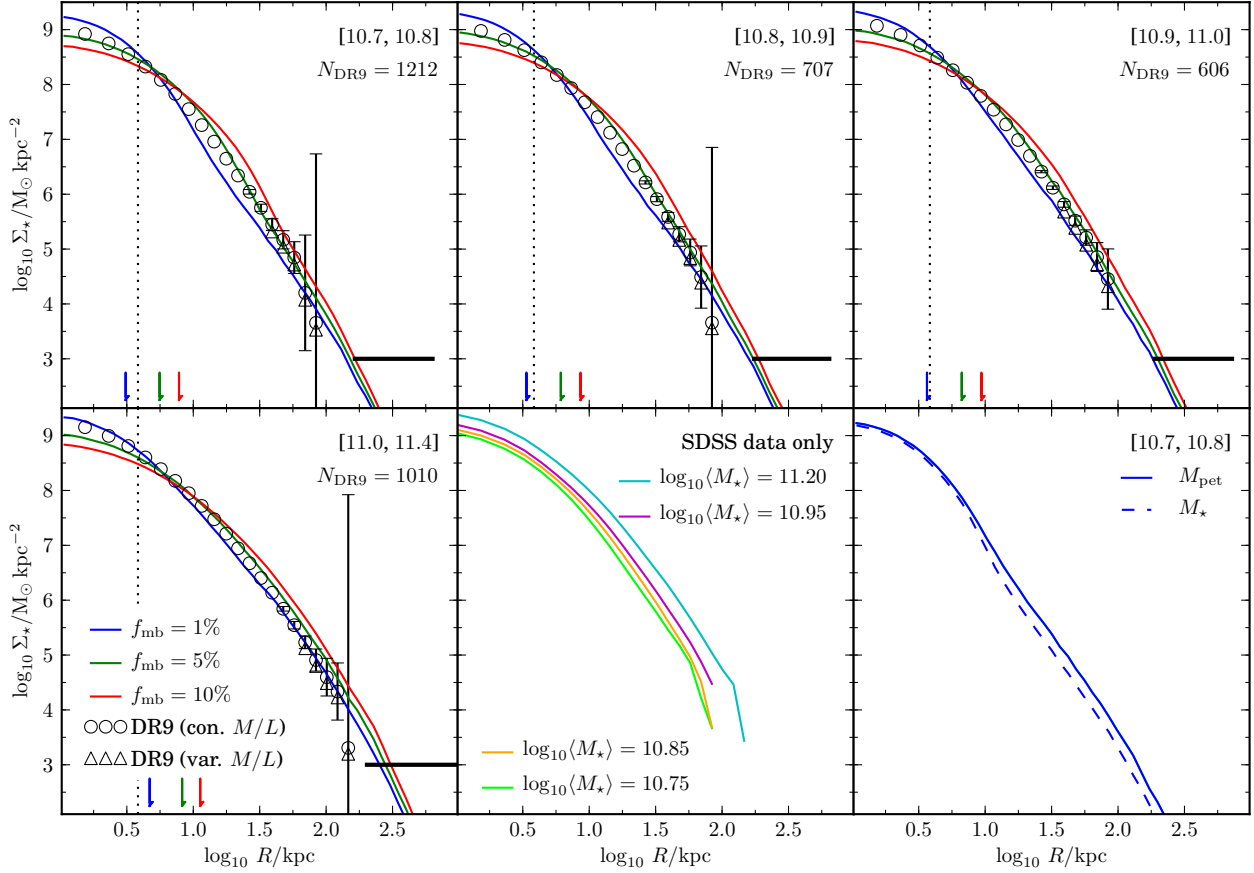
Figure 11. Symbols show the average stellar mass surface density profiles obtained from stacks of SDSS DR9 r band images as described in the text and appendix B, assuming a constant stellar mass to light ratio (open circles) and, where significantly different, a colour-dependent M/L (open triangles). Error bars approximate '1σ' of the distribution of uncertainty in the average profiles combining Poisson errors in flux measurement with the sample variance of the stack (N_{DR9} given in each panel shows the number of galaxies in the bin). Coloured lines (blue, green and red) show stacks made from our simulations as in Fig. 8 but here binning galaxies by their Petrosian mass $M_{\rm pet}$ (see text). The lower central panel shows the four SDSS profiles only (colours indicate the central mass of each bin). The lower right panel reproduces the $f_{\rm mb} = 1\%$ profile from the $[10.7, 10.8]$ panel (solid line) and compares it to the average profile of galaxies stacked in the same range of total stellar mass $M_\star$ (dashed line) rather than $M_{\rm pet}$.

Trujillo 2012) show similar profiles. All show hints of breaking to a shallower slope beyond 15–20 kpc, although these upturns occur close to the limiting depth of the observations.

In the same panel we compare with the GIMIC SPH simulations (Crain et al. 2009), the only other large cosmological simulation of stellar haloes in this M_{200} range (though see also Croft et al. 2009), with a particle mass 7.7× larger than Millennium II and the same force softening length. Font et al. (2011) stacked ∼ 400 galaxies from GIMIC. They find circularly averaged density profiles that are well described by a concentrated in situ component and a diffuse accreted component. The transition between the two components is less obvious in their profiles than in our $f_{\rm mb} = 1\%$ model, and the shallower outer slope seen in the GIMIC simulations is in better agreement with the M31 data of Gilbert et al. (2009) at ∼ 100 kpc.

In the range $13.0 < \log_{10} M/\mathrm{M}_\odot < 13.5$ accreted stars dominate the overall surface density profile. We compare with the stacked surface brightness profile of ∼ 42000 SDSS LRGs (luminous red galaxies, thought to be mostly group/cluster centrals; $M_\star \sim 10^{11}\,\mathrm{M}_\odot$, $M_{200} \sim 10^{13.2}\,\mathrm{M}_\odot$) at $\langle z \rangle \sim 0.34$ from Tal & van Dokkum (2011). These data are a good match to the surface density profiles of our simulated galaxies from 10–100 kpc. Below

10 kpc the simulated profile is steeper than the data, although this region is sensitive to our treatment of the in situ component. The simulation does not reproduce the upturn in the observed profile at ∼ 100 kpc, which Tal & van Dokkum (2011) attribute to limitations in their correction for residual light from unresolved companion galaxies. Our model supports this interpretation because it does not predict a separate physical component with a shallow density profile that could explain the upturn. We also show the stacked profiles of 14 nearby early type galaxies from the volume-limited OBEY survey (Tal et al. 2009). This stack includes all ellipticals in the survey with stellar mass $\log_{10} M_\star/\mathrm{M}_\odot = 11.45 \pm 0.15$ (appendix D of van Dokkum et al. 2010). These data match the Tal & van Dokkum (2011) stack at small radii and do not show an excess over our simulated profile at $R \gtrsim 100$ kpc, possibly because van Dokkum et al. (2010) stack 2D fits to the OBEY galaxies rather than stacking the images directly.

Finally, the most massive haloes in our simulation have $13.5 < \log_{10} M_{200}/\mathrm{M}_\odot < 14.0$. We compare these with individual BCG profiles from Kormendy et al. (2009, M87) and Seigar et al. (2007, Abell cluster cD galaxies; we plot their 'double Sèrsic' fits). Our simulations match these profiles well from 10–100 kpc, although some of the observed galaxies could belong to haloes

more massive than the median of our bin (e.g. $\log_{10} M_{200}/\mathrm{M}_\odot = 15.1$ for NGC 4874/Coma and 14.3 for UGC 9799/Abell 2052; Reiprich & Böhringer 2002). We also show the results of Zibetti et al. (2005) who stacked SDSS images for BCGs at $\langle z \rangle \sim 0.25$. This is deeper than any of the individual profiles and shows a clear excess over our models beyond 100 kpc. Some of this disagreement may be due to a mismatch in the average M_{200} of the galaxies being compared, as mass–richness relations suggest that the typical halo mass of the Zibetti et al. sample is $M_{200} \gtrsim 10^{14.2}\,\mathrm{M}_\odot$ (e.g. Rozo et al. 2009). It may also indicate that effects neglected by our model become important in this regime. For example, it may be that the angular momentum of disc galaxies affects the orbital energy distribution of their tidal tails, or that ram-pressure stripping of cold gas leads to more rapid disruption of satellites; in both cases, more stripped stars would be deposited on weakly bound orbits with large apocentres.

6 COMPARISON WITH STACKED SDSS DATA

It is more appropriate to compare the average galaxy surface density profiles from our models with similar averages constructed from large galaxy samples (such as the stacking analyses of Tal & van Dokkum 2011 and Zibetti et al. 2005) than with individual galaxies or small surveys as we did in the previous section. We have carried out our own simple stacking analysis of massive galaxies observed by the Sloan Digital Sky Survey (SDSS) Data Release 9 (DR9; Ahn et al. 2012) in bins of stellar mass (as given by the MPA-JHU Value-Added Catalogue[8]). Our method for constructing stacked images is described in appendix B.

The resulting density profiles are shown as open circles in Fig. 11, split into four bins of stellar mass, each of which is obtained from a stack of N_{DR9} galaxies as indicated. The panel labelled 'SDSS data only' summarises these four profiles, showing a clear shift in amplitude from the least to the most massive bin, out to the largest measured radius. Each panel assumes a constant r band mass-to-light ratio (the average of the MPA-JHU M/L_r values in the corresponding MPA-JHU mass bin, ranging from 2.3 to 2.8 from the first to last bin; see appendix B) but this result holds even if the same M/L_r is used for all panels, or if a colour-dependent M/L_r relation is used (Bell et al. 2003). However, the stacked observational data do not show any significant change in profile shape of the kind seen in previous figures (including observations of individual galaxies).

Each panel compares our SDSS stacks to the average profiles of simulated galaxies[9] binned by their Petrosian stellar mass, M_{pet} (blue, green and red lines for $f_{\mathrm{mb}} = 1\%, 5\%$ and 10%, respectively). We use M_{pet} rather than the true stellar mass $M_\star$ in order to reproduce approximately the bias introduced by SDSS `modelMag` magnitudes, from which the MPA-JHU masses are derived (see appendix B). M_{pet} is always an underestimate of $M_\star$, thus the galaxies included in each bin of Fig. 11 are different from those in the corresponding bin of Fig. 8. The result is a small systematic increase in the amplitude of the average density profile, by up to ~ 0.5 dex at large radii. This effect is most evident in the $10.7 < \log_{10} M_{\mathrm{pet}} < 10.8$ bin for $f_{\mathrm{mb}} = 1\%$, where it obscures

the inflection seen in Fig. 8 (see lower right panel of Fig. 11). The weakness of the overall trend in Fig. 11 compared to that in Fig. 6 is mainly due to scatter between $M_\star$ and M_{200} (see Fig. 8). For example, the bin $10.7 < \log_{10} M_\star < 10.8$ corresponds to a ~ 1.5 dex range in M_{200}.

Even though the trends in the simulated data are quite weak, for $f_{\mathrm{mb}} = 1\%$ they are still clearly stronger than observed. For $f_{\mathrm{mb}} = 5\%$, on the other hand, the agreement with observation is quite good, and a slightly smaller value of f_{mb} would agree even better, consistent with our findings in Section 2.4.

7 ORIGIN AND STRUCTURE OF STELLAR HALOES

Having demonstrated that our particle-tagging model produces surface density distributions that agree reasonably well with observations, we now use it to examine the origin of stellar haloes as well as the relationships between the properties of central galaxies and the structure of their diffuse light.

The left panel of Fig. 12 shows M_{acc}, the total mass of accreted stars in each of our galaxies, as a function of virial mass, M_{200}. The right panel shows M_{acc} as a function of the total stellar mass of the system, $M_\star$. M_{acc} increases much less steeply with M_{200} above a characteristic mass $M_{200} \sim 10^{12.5}\,\mathrm{M}_\odot$. This corresponds roughly to the transition mass predicted by the G11 model, above and below which the galaxy mass function is dominated by early and late type galaxies respectively. We see in Fig. 12 that elliptical (G11 $B/T > 0.9$) and late type galaxies have a clean separation at an accreted stellar mass of $M_{\mathrm{acc}} \sim 3 \times 10^{10}\,\mathrm{M}_\odot$, which (as shown in the right panel of Fig. 12) corresponds to ~ 30 per cent of the total (accreted plus in situ) central galaxy stellar mass $M_\star$ (for all M_{200}). This simply reflects the fact that the 'major merger' criterion for the destruction of discs (hence formation of elliptical galaxies) in G11 is a progenitor mass ratio of 1:3 or lower.

Purcell et al. (2007) made similar predictions for M_{acc} as a function of M_{200} at $z = 0$ using prescriptions for halo assembly histories and subhalo orbital properties based on numerical simulations. As their results demonstrated, the relationship between M_{acc} and M_{200} seen in Fig. 12 is a natural outcome of the CDM progenitor halo mass function and the relation between $M_\star$–M_{200}, which is thought to be roughly monotonic (e.g. White & Frenk 1991; Benson et al. 2000; van den Bosch, Yang & Mo 2003). To first order, this means that M_{acc} is set by the typical ratio of M_{200} between the few most massive accreted progenitors and the main halo (~ 0.1–1%). However, $M_\star$–M_{200} relations derived from galaxy abundance matching (like those predicted by semi-analytic models) show an inflection corresponding to a peak in galaxy formation efficiency at $M_{\mathrm{peak}} \approx M_{200} \sim 10^{12}\,\mathrm{M}_\odot$ (e.g. Eke et al. 2004; Conroy, Wechsler & Kravtsov 2006; Vale & Ostriker 2006; Guo et al. 2010; Moster et al. 2010). This creates two regimes in the scaling of M_{acc} with M_{200}.

In haloes with $M_{200} \lesssim M_{\mathrm{peak}}$, in situ star formation efficiency per unit halo mass increases steeply along the halo mass function, up to a maximum around the Milky Way mass (e.g. Moster et al. 2010). Because even the most massive accreted haloes typically have much lower galaxy formation efficiency than the main halo, M_{acc} remains a small fraction of $M_\star$ and depends strongly on M_{200}[10]. For $M_{200} \gtrsim 10 M_{\mathrm{peak}}$, the most massive progenitor haloes have a galaxy formation efficiency comparable to or

---

[8] http://www.mpa-garching.mpg.de/SDSS/DR7
[9] The observed and simulated profiles in Fig. 11 should only be compared at $R \gtrsim 5$ kpc. At smaller radii, the point spread function, which we have not deconvolved, dominates the observed profiles and numerical softening affects the simulated profiles.

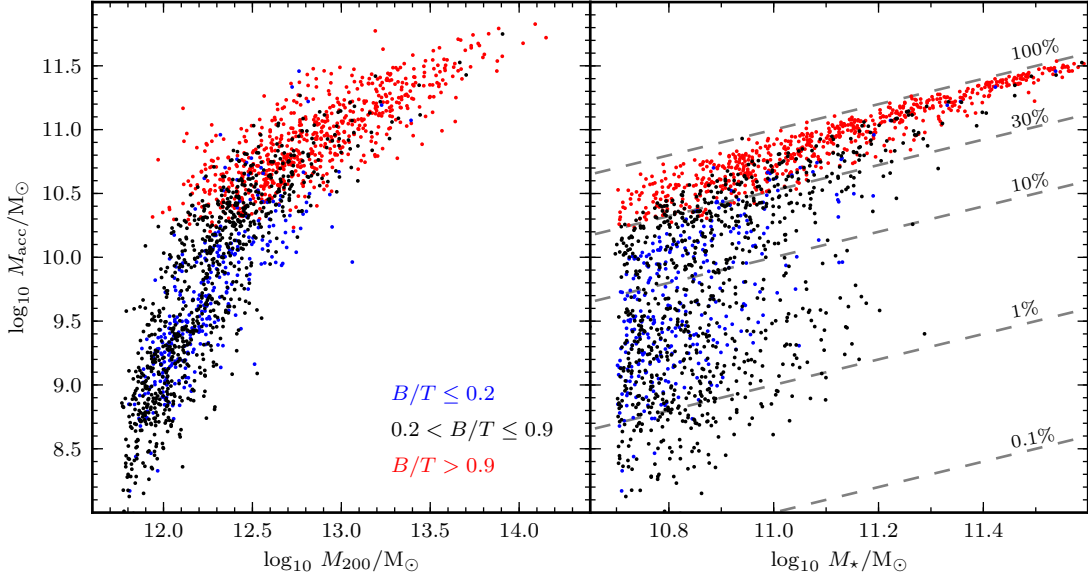[10] In the extreme case, sharp thresholds for galaxy formation at very low

Figure 12. Left: points show the total mass of accreted stars, M_{acc} as a function of M_{200}, split by bulge-to-total ratio as shown in the legend. Right: points show M_{acc} as a function of stellar mass, $M_\star$. Grey lines correspond to fractions of the total stellar mass as indicated.

even higher than the main halo and M_{acc} makes up a much larger fraction of $M_\star$. However, as the $M_\star-M_{200}$ relation flattens, the number of progenitors continues to scale with M_{200}, but the stellar mass per massive progenitor does not. The result is that M_{acc} scales more slowly with M_{200} than it does below M_{peak}.

In the G11 model, lower galaxy formation efficiency above M_{peak} is the result both of longer cooling times and of AGN feedback (Kauffmann & Haehnelt 2000; Croton et al. 2006; Bower et al. 2006). This model follows the entire hierarchy of galaxy formation and, with particle tagging, we have now computed the dynamical evolution of all satellite disruption events in that model directly from Millennium II. These techniques mean that our model is significantly more accurate and detailed than the empirical $z = 0$ scaling relations used by Purcell et al. (2007), so it is useful to revisit their analysis. Fig. 13 presents the data from Fig. 12 in the same way as figure 4 of Purcell et al. (2007), showing the ratio of M_{acc} to $M_\star$ as a function of M_{200}. As expected, our results are qualitatively similar[11] to Purcell et al.. However, our model predicts a significantly steeper relation: an average accreted stellar mass fraction of 30 per cent is reached in haloes with $M_{200} \sim 10^{12.5} M_\odot$ rather than $M_{200} \sim 10^{13.5} M_\odot$.

Both models appear roughly consistent with the (limited) data on late type galaxies in haloes of $M_{200} \sim 10^{12} M_\odot$, represented in Fig. 13 by M31 (black point; Watkins et al. 2010; Courteau et al. 2011) and the Milky Way (grey box; Smith et al. 2007; Bell et al. 2008; Li & White 2008). In order to compare M_{acc} in our results and in those of Purcell et al. to these observations in Fig. 13, we have assumed that all observed halo stars are accreted while all disc and bulge stars formed in situ. If this assumption is reasonable,

M_{200} (the atomic hydrogen cooling limit, reionization etc.) will result in central galaxies that do not accrete any luminous progenitors and have $M_{acc} = 0$.

[11] Purcell et al. (2007) define their virial quantities at an overdensity of $\Delta = 337$ rather than $\Delta = 200$ as we do. We have not corrected their results for this difference in Fig. 13; doing so would shift their curves to the right (higher virial mass) by $\lesssim 0.1$ dex for plausible NFW concentrations.
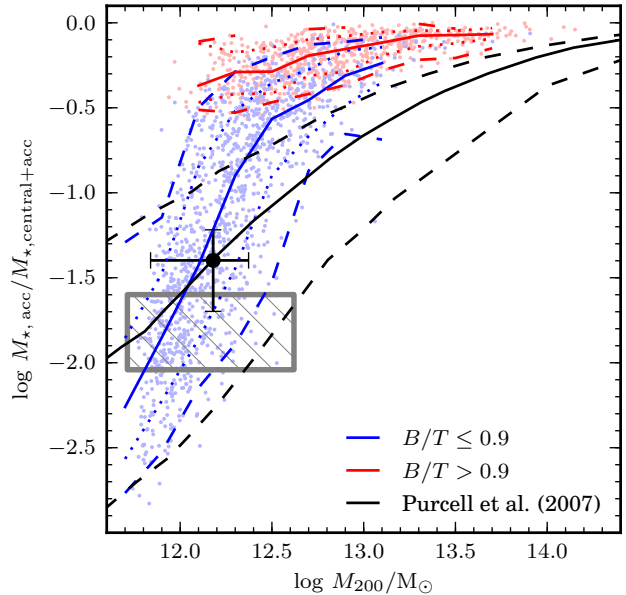

Figure 13. Solid blue and red lines show the median ratio of accreted stellar mass (both halo and bulge) to the total galaxy mass (sum of accreted and in situ stars). Colours separate galaxies by B/T as given in the legend. Dashed lines of the same colour enclose 90 per cent of the distributions. Black solid and dashed lines correspond to the same quantities for the distribution shown in figure 5 (left panel) of Purcell et al. (2007). Grey hatching and the black point with errorbars indicate likely values for the Milky Way (Smith et al. 2007; Li & White 2008; Bell et al. 2008; McMillan 2011) and M31 (Watkins et al. (2010); Courteau et al. (2011) respectively.)

Fig. 13 may imply that the Milky Way has a less massive stellar halo than the average for its likely halo mass, or that the lower values of M_{200} are preferred. Fig. 13 reinforces the conclusion of C10 that considerable scatter is expected in M_{acc} for Milky Way–like galaxies. C10 attributed this to scatter in the accretion time and

mass of the most massive progenitor satellite (in the Milky Way, for example, the Sagittarius dwarf has contributed to the stellar halo, but the Large Magellanic Cloud has not).

Our model disagrees with Purcell et al. (2007) at higher M_{200}, where most galaxies are ellipticals and even a lower limit to the accreted component is hard to identify by decomposing the light profile. Our model predicts that a late type galaxy in a halo of $10^{13} M_\odot$ should have ~ 30 per cent of its total stellar mass in an extended $n \sim 3$–4 spheroid of accreted stars (Purcell et al. predict ~ 10 per cent). This can be tested with deep images of nearby massive disc galaxies (including S0s) for which the total mass is well constrained by the rotation curve.

Finally, we discuss the progenitor galaxies that contribute stars to the accreted component in our models. A progenitor is defined as a galaxy that is disrupted within the 'main branch' of a halo merger tree – each progenitor may have many progenitors of its own, but all these are grouped together in this definition based on only the final level in the hierarchy. Following the definition given in section 4 of C10, we find the most massive galaxies in our sample typically have ~ 10 significant progenitors to their accreted component (see also Laporte et al. 2012). Ellipticals have a reasonably tight correlation between the number of significant progenitors and M_{200}; the lowest mass ellipticals in our sample typically result from a single major merger and thus have only one significant progenitor. Late type galaxies have a larger scatter in the number of significant progenitors of $M_{\rm acc}$. They can be dominated by one massive object, in agreement with the findings of C10, but we also find cases with 10 or more significant progenitors.

The left-hand column of Fig. 14 shows the mass of the most massive progenitor in each of our galaxies. The upper and lower panels of this plot separate two classes of progenitor, according to where their stars settle in the main halo after they have been accreted. We define 'bulge' progenitors to be those that deposit more than half their stars within a radius of 3 kpc from the centre of the main halo at $z = 0$. The rest are classified as 'stellar halo' progenitors (the same definition was used in C10).

The most massive 'bulge' progenitor is typically the most massive of all accreted galaxies, which is not surprising because more massive satellites suffer more dynamical friction and sink quickly to the centre of the potential. Thus the relation between the mass of the most massive bulge progenitor and the mass of the dark halo is similar to that shown in Fig. 12, with a steep slope for late-type galaxies and an approximately constant value for ellipticals. On the other hand, the mass of the most massive stellar halo progenitor shows the same trend with M_{200} in both late types and ellipticals. Thus our model predicts the outer stellar haloes of all galaxies to be equally diverse at fixed M_{200}. The most massive bulge progenitor is ~ 10 times as massive as the most significant contributor to the halo up to $M_{200} \sim 10^{13} M_\odot$; at higher M_{200} the most significant bulge and stellar halo progenitors have similar mass.

The right-hand column of Fig. 14 shows the mass of the most massive bulge and halo progenitors as a fraction of the total accreted stellar mass of the main galaxy in the same region. The accreted bulges of late type galaxies usually acquire at least ~ 40 per cent of their stars from one progenitor, reaching $\gtrsim 90$ per cent in many cases. On the other hand, the most massive contributor to the accreted stellar halo typically accounts for no more than ~ 30 per cent of its total mass, and rarely exceeds 50 per cent. In more massive galaxies ($M_\star \gtrsim 10^{11.2} M_\odot$, which mostly have G11 $B/T > 0.9$) we find very few cases where more than 70 per cent of accreted bulge or halo stars originate in a single progenitor. As dis-
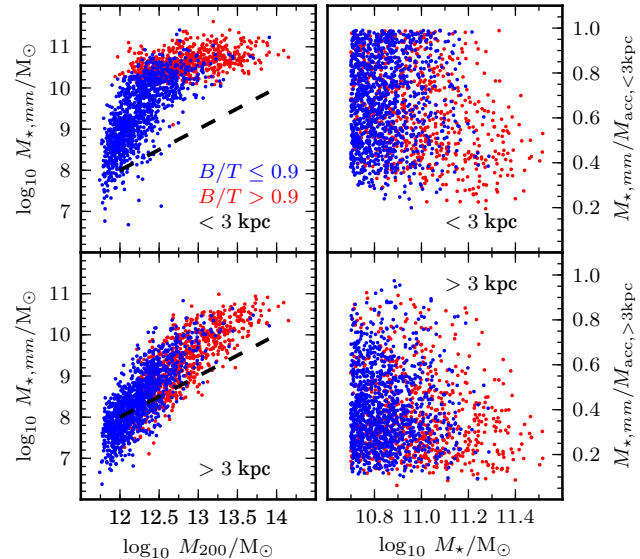

Figure 14. The stellar mass of the most massive progenitor, $M_{\star,mm}$, as a function of total halo mass M_{200} (left) and the fraction of stellar mass accreted from the most massive progenitor as a function of galaxy stellar mass $M_\star$ (right). Upper and lower panels separate progenitors by the half mass radius r_{50} of their stellar debris at $z = 0$: $r_{50} < 3$ kpc (the 'bulge') and $r_{50} > 3$ kpc (the 'stellar halo'), respectively. The dashed black lines in the left-hand panels show the mass corresponding to $1 \times 10^{-4} M_{200}$.

cussed above, progenitors with $M_{200} > M_{\rm peak}$ (the most efficient halo mass for galaxy formation) have roughly the same stellar mass as the central galaxy that accretes them. This means that massive ellipticals can undergo mergers that are 'minor' in terms of M_{200} (and thus numerous) but 'major' in terms of accreted stellar mass.

8 CONCLUSIONS

We have used dark matter particles in the Millennium II simulation as dynamical tracers of stellar populations, in order to study the hierarchical assembly of galactic structure in the CDM model. We have constrained the free parameter of our particle tagging method, $f_{\rm mb}$, by comparison to the galaxy mass–size relation for late-type galaxies and find acceptable values in the range $1\% < f_{\rm mb} < 5\%$. We have identified several limitations in the treatment of the in situ component that could be improved on in future work (see Section 2.5). In particular, the approximation of a universal constant value of $f_{\rm mb}$ could be removed by computing it from other quantities in our semi-analytic model.

Our most important conclusions can be summarised as follows:

(i) The stellar mass surface density profiles of galaxies in our model are well described by the sum of two Sèrsic models, corresponding to the separate contributions of stars formed in situ and stars accreted from other galaxies.

(ii) The surface density of in situ stars falls off more rapidly with radius than the accreted component. In situ stars only make a significant contribution to surface brightness profiles out to $R \sim 10$ kpc in $M_{200} \sim 10^{12} M_\odot$ halos or 40 kpc in $M_{200} \sim 10^{14} M_\odot$ haloes for $f_{\rm mb} \sim 1\%$.

(iii) The outer isophotes of all massive galaxies are dominated by accreted stars, which extend to the virial radius in most systems.

(iv) Stellar mass surface density profiles show very little scatter from galaxy to galaxy at fixed M_{200}, particularly in group-scale haloes ($M_{200} > 10^{13.5}\,\mathrm{M_\odot}$). This is the consequence of strong correlations between halo mass, central star formation efficiency and the galaxy progenitor mass function, and is a basic feature of galaxy formation in the CDM model (e.g. Purcell et al. 2007). Comparison at fixed $M_\star$ shows more scatter, because of scatter in the relationship between $M_\star$ and M_{200}.

(v) The stellar content of galaxies can be in situ dominated or accretion dominated. Accretion-dominated galaxies have more extended profiles and higher Sèrsic index than in situ-dominated galaxies. They have approximately 'power law' profiles from 10–100 kpc that show no clear inflection at the transition between in situ and accreted components and are associated with haloes that host elliptical galaxies, according to the criteria described by G11. These massive haloes have usually been subject to 'major' mergers (violent relaxation) after $z \sim 1$, which reshape their in situ component. They also suffer strong suppression of star formation by AGN feedback which prevents a compact core of in situ stars forming at low redshift.

(vi) In situ dominated profiles are typical of less massive haloes (up to $M_{200} \sim 10^{13}\mathrm{M_\odot}$). In situ stars have a compact exponential distribution by construction in our model. Extended ($R_{50} \sim$ 10 kpc) accreted spheroids begin to dominate only at $R \gtrsim 10$ kpc, causing a clear inflection in the circularly-averaged surface brightness profile. Neither compact bulges nor compact exponential elliptical galaxies are created by accretion in our model.

(vii) The transition from in situ dominated profiles to accretion dominated profiles with increasing M_{200} is less clear when studied in terms of central stellar mass $M_\star$, because of scatter in the $M_\star$–M_{200} relation in our model.

(viii) The central galaxies of massive groups and clusters typically have ~ 10 accreted progenitors with similar stellar masses. In contrast, the bulges of less massive haloes are dominated by one progenitor, typically the most massive of those accreted; their stellar haloes are more diverse. The scatter in the number of significant progenitors of bulges and stellar haloes is larger at lower M_{200}. The progenitor mix is not significantly different in the stellar haloes of late and early type galaxies in our model. All these findings are readily explained by trends in star formation efficiency with halo mass in the ΛCDM model.

(ix) We have compared the results of our model with data from the literature, including deep surface brightness profiles of individual galaxies and stacks of LRGs and BCGs. Subject to the crude way in which we have assigned galaxies to halo mass bins and our simplification of a constant mass-to-light ratio, the range of shapes, amplitudes and scales seen in our simulated surface density profiles for accreted stars agree qualitatively with these observations.

(x) We have stacked SDSS images of galaxies in bins of stellar mass to obtain average surface density profiles that can be compared directly to the results of our simulations. We find a weak trend of surface density amplitude with $M_\star$ but no clear change in profile shape. We find this is also the case in our simulations, once we account for the well-known bias in stellar mass measurements for massive galaxies due to the finite depth of SDSS photometry.

The next generation of deep sky surveys (culminating in LSST) will reach the low surface brightness limits required to detect stellar haloes and accretion remnants around the majority of low-redshift $L_\star$ galaxies. The dawn of this new era in the observation of galaxy structure is a strong motivation for the further study of these regions in simulations. We have shown that the particle tagging technique is a straightforward and well-constrained extension of the semi-analytic method with a number of interesting applications that merit further investigation. These include stellar population gradients in early-type galaxies; the kinematics of diffuse light; the effects of interactions on the structure of satellite galaxies and environmental trends; the frequency of tidal features and their correlations with other galaxy properties; and the intracluster light of massive clusters.

APPENDIX A: DIFFERENCES WITH C10 AND NUMERICAL CONVERGENCE

There are a number of minor differences between the tagging procedure we use on Millennium II and that used on the Aquarius simulations by C10. First, as discussed at length in the main text, we now tag particles to represent in situ stars in our 1872 target central haloes as well as those formed in their progenitors and satellite galaxies. In C10, the distribution of in situ stars in the main halo
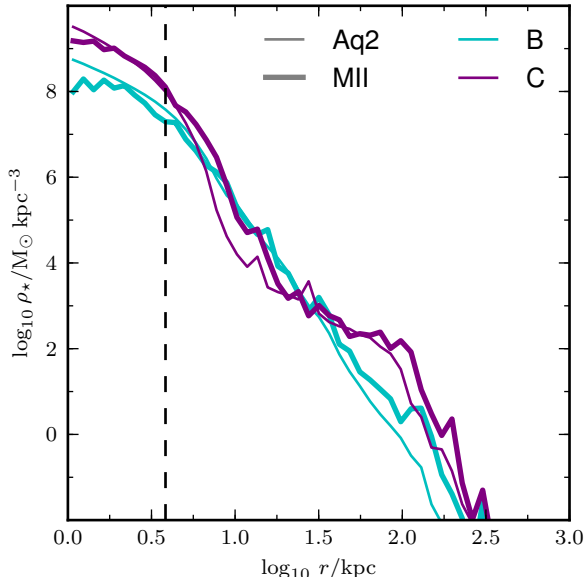
Figure A1. Comparison between particle-tagging stellar mass surface density profiles in Aquarius haloes B (cyan) and C (purple) at dark matter mass resolutions of $\sim 1 \times 10^3 \, \mathrm{M_\odot}$/particle (thin lines, Aquarius level 2) and $6.8 \times 10^6 \, \mathrm{M_\odot}$/particle (thick lines, Millennium II). The softening length of Millennium II is shown by the vertical dashed line. These profiles differ from those shown by C10 because they are based on the G11 semi-analytic model and also include the in situ component.

was not considered, but only because they were not the focus of that paper and excluding them made the computation less demanding.

Second, the semi-analytic component of our model must deal with galaxies in dark matter haloes that fall below the mass resolution limit of the simulation because of tidal stripping. We do this in the same way as G11, by estimating the time for inspiral of the satellite due to dynamical friction in its parent halo, and merging it with the central galaxy after that time. The satellite can also be disrupted sooner if its density falls below that of the dark halo at the satellite's pericentre. This approach differs from C10, where galaxies in unresolved subhalos were merged instantly with the main galaxy in their parent halo (in which case the disruption of the N-body subhalo is equivalent to the disruption of the galaxy, as it would be in an SPH simulation with collisionless star particles). C10 did this because of the high resolution of their Aquarius simulations, which meant that it made almost no difference to their results. However, at the lower resolution of Millennium II, allowing galaxies to survive after the disruption of their N-Body subhalos is necessary for convergence of the semi-analytic model and its agreement with observations (details are given in G11; see also Font et al. 2011). Therefore, our tagging method must make allowance for new stars forming in galaxies with unresolved haloes. We do this by tagging those stars to a single particle, the most-bound particle of the halo at the time it was last resolved. Because very few stars form in such haloes, this makes no practical difference.

There is a more significant issue related to the treatment of semi-analytic galaxies with unresolved haloes. Our analysis (for example, in constructing density profiles) treats the stars in these galaxies as having been stripped, because their dark matter par-

ticles are bound to the main dark matter halo. This includes the most-bound particle to which we tag any residual star formation. Again, this treatment is similar to conventional hydrodynamic simulations, which usually do not track galaxies below the resolution limit. However, because of this, our definitions of stellar mass are not consistent between the semi-analytic model (where these all stars belong to a galaxy) and our tagged-particle model (where they are all stripped). These ambiguous stars are easy to identify in the model, and we have verified that this choice makes no significant difference to our results.

A related problem is that the lower resolution of Millennium II (relative to the Aquarius simulations of C10) makes *all* satellite galaxies somewhat easier to disrupt (at fixed mass), because their density is artificially reduced at radii below the force softening scale. Finally, it may be the case that Millennium II does not resolve a significant number of faint progenitors at all, particularly for the least massive main galaxies in our sample. However, as the much higher resolution simulations of C10 have shown, most of the stellar mass accreted by Milky Way mass haloes comes from a small number of their most massive progenitors, which are well resolved in Millennium II. In Fig. A1 we compare the high-resolution Aquarius simulations of C10 with the same haloes simulated at the resolution of Millennium II. We find that resulting stellar mass density profiles have converged above the softening scale of Millennium II. The details of profile shape that distinguish different Aquarius haloes in C10 are reproduced in Millennium II, which has a particle mass almost four orders of magnitude larger. This is the case for both the accreted and in situ components. This implies that the resolution effects described above are not very important for our results (and notably, that the underlying semi-analytic model of G11 has also converged with regard to the predicted stellar mass of the Aquarius progenitors).

The final difference with C10 is that we do not postpone the tagging process to later snapshots in cases where the target halo is deemed to be out of equilibrium. Although well-motivated, C10 found that this procedure makes the implementation of the method much more complex but has little influence on the outcome[12]. Other technical subtleties, including tagging a fixed number of particles rather than a fixed fraction in subhalos that are losing mass, are dealt with as described in C10.

APPENDIX B: SDSS STACKING ANALYSIS

In Section 6 we stacked galaxies from SDSS DR9 for comparison with our models. This appendix describes our method for selecting galaxies in SDSS and stacking their images. We intend to explore a number of important systematic uncertainties in more detail and present further results in a separate paper (D'Souza et al. in preparation), so our analysis here should be considered preliminary.

Our starting point is the MPA-JHU SDSS 'value-added' catalogue, which provides an estimate of stellar mass for galaxies with spectra in DR7 based on fitting an SED to their `modelMag` photometry (Kauffmann et al. 2003a; Salim et al. 2007). From this catalogue, we selected isolated central galaxies in the redshift range $0.07 < z < 0.08$ by applying the criteria of Wang & White (2012): a galaxy of apparent r band magnitude m is considered isolated if there are no galaxies in the spectroscopic catalogue at a projected

---

[12] At the level of the other approximations in this method, it is arguable that allowing assignments to non-equilibrium haloes might be a reasonable representation of the messy nature of star formation in mergers.

radius $R < 0.5\,\mathrm{Mpc}$ and velocity offset $|\delta z| < 1000\,\mathrm{km\,s^{-1}}$ with magnitude $m' < m + 1$, and none within $R < 1\,\mathrm{Mpc}$ and $|\delta z| < 1000\,\mathrm{km\,s^{-1}}$ with $m' < m$. We make no selection on colour or morphological type.

We created $1\,\mathrm{Mpc^2}$ mosaics in the g, r and i bands centered on each galaxy in our sample using the 'corrected' sky-subtracted frames from the SDSS Data Release 9 image server and SWarp (Bertin et al. 2002). These three mosaics were stacked together to make a 'master image' from which a 'master mask' was obtained using SExtractor (Bertin & Arnouts 1996). Other galaxies in the field were conservatively masked by convolving the master image with an 8×8 pixel top hat kernel before running SExtractor. The master mask was applied to each individual mosaic. The masked mosaics were then transformed to $z = 0.08$ with the flux-conserving IRAF task geotran, cropped to a uniform size of 1200×1200 pixels (690×690 kpc at $z \sim 0.08$) and corrected for extinction following Schlegel, Finkbeiner & Davis (1998).

We assume that the sky subtraction provided by the SDSS imaging pipeline is adequate for our analysis. The pipeline sky subtraction was known to have shortcomings in early data releases, but was revised in DR8[13] to improve the photometry of extended low-surface brightness regions around low redshift galaxies (Blanton et al. 2011). We confirmed the quality of the sky subtraction in the DR9 images by carrying out tests using the earlier DR7 images with our own background subtraction, and also by comparing DR9 surface brightness profiles for galaxies in the Virgo cluster with the results of Kormendy et al. (2009).

We binned our SDSS sample for stacking in mass bins as we did our simulations in Fig. 10, using the mode of the MPA-JHU mass PDF corrected to a Hubble parameter $h = 0.73$ for consistency with the cosmology of our simulations[14]. This resulted in $\sim$ 600–1200 SDSS galaxies per bin. Mosaics in the gri bands were stacked separately using IRAF imcombine, taking the mean value[15] of each pixel after clipping at the 10th and 90th percentiles. Images were centered before stacking but were not axis-aligned. We also removed a small residual background from each stack such that the stellar mass surface density falls to zero at the periphery of the mosaic. The g, r and i band mosaics for each galaxy were not included in the corresponding stacks if they included stars brighter than $r = 12$, if they fell in the upper 10th percentile of the distribution of pixel RMS for each mosaic in their mass bin, if they had more than 75% of their central 60 arcseconds masked, or if the masking algorithm failed due to a crowded field.

In a given mass bin, the azimuthally averaged mass profile was derived from the r band stack assuming a constant mass-to-light ratio. The M/L_r assumed for each bin is the average of M/L for the galaxies in the bin, derived from their MPA-JHU mass and r band modelMag; in order of $M_\star$ for the four bins, $M/L_r = [2.154, 2.240, 2.391, 2.516]$. We also used the g, r and i stacks to derive a radially varying M/L_r profile based on the colour of the light in each annulus, using the prescriptions of Bell et al. (2003) with a Chabrier IMF. This only makes a significant difference in the outermost radial bins of each profile. However, the potential for large colour errors at faint magnitudes (particularly those involving the i band) adds considerably to the uncertainty in these radially varying profiles.

We have not carried out deconvolution of the PSF at any stage of our analysis. Galaxies in the mass and redshift range of our sample are typically well resolved, so the PSF mostly affects the very inner part of the light profile. We have compared the profiles of individual galaxies in our stacks with similar galaxies at lower redshift, with SDSS profMean profiles and with deep data from the Virgo cluster (Kormendy et al. 2009) to verify that the PSF only has a significant effect (very roughly, of the order of $\gtrsim 0.1$ magnitudes per square arcsecond in the surface brightness profile) at $R \lesssim 5$ kpc. Nevertheless, particularly for the i band magnitude and the measurement of colours, PSF effects are known to be significant at much larger radii (de Jong 2008) and a complete analysis should include a more thorough quantification of the PSF (e.g. Tal & van Dokkum 2011).

We estimated the uncertainty in each annulus in the constant M/L case as the sum in quadrature of Poisson error in the flux per contributing pixel and the average RMS pixel-by-pixel deviation of each image from the stack in that annulus, the latter term accounting for the sample variance. A bootstrap estimate of variance would be preferable to understand the effects of sample variance, but proved to be computationally expensive. Bootstrapping on sub-samples of 100 galaxies suggested that our algorithm underestimates the variance in the outer regions of the profile by a factor of 2, so we multiply our variance estimate by 2 to obtain the error bar in Fig.11. This crude estimate of uncertainty is sufficient to indicate the largest radius to which each stacked profile is robust, but it could be made substantially more accurate with further work.

In our selection of SDSS galaxies for stacking, we have used the MPA-JHU stellar mass estimates. These masses are derived from the galaxy modelMag magnitude, which attempts to correct for undetected light in regions of low surface brightness by fitting the observed surface brightness profile to one of two analytic models (exponential and $r^{1/4}$) and adopting the total magnitude of the best fit. However, because the fits are to truncated light profiles (owing to the finite surface brightness limit, of more importance for more extended galaxies) and assume a fixed Sèrsic index $n = 4$ for the early-type model, they are likely to suffer from a bias relative to the true total light similar to that of the Petrosian magnitude petroMag. In theory petroMag is a substantial underestimate of the total light for galaxies with Sèrsic index $n \gtrsim 4$, but includes almost all of the light for galaxies with $n \sim 1$ (Graham et al. 2005; Lauer et al. 2007; Blanton et al. 2011).

The bias in modelMag is more difficult to reproduce in our simulations because it depends on the fitting process itself (for example, in the behaviour of fits to multi-component galaxies, or with substantial noise). Furthermore, we find that the median offset between modelMag and petroMag for galaxies in our SDSS sample is generally small (~ 0.1 magnitudes). We therefore compute the 'Petrosian' mass from the simulations and use this as a proxy for the SDSS modelMag mass in Fig. 11. We do so with an algorithm analogous to that used for Petrosian flux reported by SDSS (i.e. the mass within $2r_p$, using the same definition of r_p). The resulting M_{pet} underestimates $M_\star$ for the most massive galaxies, thereby redistributing galaxies with high-n profiles to lower mass bins in our simulated stacks.

---

[13] See www.sdss3.org/dr9/imaging/images.php and www.sdss3.org/dr9/imaging/caveats.php

[14] We have not accounted for a possible overestimate of the DR7 modelMag magnitudes owing to uncertainties in the background subtraction of extended galaxies pre-DR8.

[15] Median and mode stacking produced very similar results.

REFERENCES

Abadi M. G., Navarro J. F., Steinmetz M., 2006, MNRAS, 365,

747

Ahn C. P., Alexandroff R., Allende Prieto C., Anderson S. F., Anderton T., Andrews B. H., Aubourg É., Bailey S., et al., 2012, ApJS, 203, 21

Baade W., 1944, ApJ, 100, 147

Bailin J., Bell E. F., Chappell S. N., Radburn-Smith D. J., de Jong R. S., 2011, ApJ, 736, 24

Bakos J., Trujillo I., 2012, ArXiv e-prints, astro-ph/1204.3082

Barker M. K., Ferguson A. M. N., Irwin M., Arimoto N., Jablonka P., 2009, AJ, 138, 1469

Barker M. K., Ferguson A. M. N., Irwin M. J., Arimoto N., Jablonka P., 2012, MNRAS, 419, 1489

Baugh C. M., Cole S., Frenk C. S., 1996, MNRAS, 283, 1361

Baugh C. M., Lacey C. G., Frenk C. S., Granato G. L., Silva L., Bressan A., Benson A. J., Cole S., 2005, MNRAS, 356, 1191

Bell E. F., McIntosh D. H., Katz N., Weinberg M. D., 2003, ApJS, 149, 289

Bell E. F., Wolf C., Meisenheimer K., Rix H.-W., Borch A., Dye S., Kleinheinrich M., Wisotzki L., et al., 2004, ApJ, 608, 752

Bell E. F., Zucker D. B., Belokurov V., Sharma S., Johnston K. V., Bullock J. S., Hogg D. W., Jahnke K., et al., 2008, ApJ, 680, 295

Belokurov V., Zucker D. B., Evans N. W., Gilmore G., Vidrih S., Bramich D. M., Newberg H. J., Wyse R. F. G., et al., 2006, ApJ, 642, L137

Bender R., Burstein D., Faber S. M., 1992, ApJ, 399, 462

Benson A. J., Bower R., 2010, MNRAS, 405, 1573

Benson A. J., Cole S., Frenk C. S., Baugh C. M., Lacey C. G., 2000, MNRAS, 311, 793

Benson A. J., Devereux N., 2010, MNRAS, 402, 2321

Bernardi, M., Meert, A., Sheth, R. K., Vikram, V., Huertas-Company, M., Mei, S., Shankar, F., 2013, ArXiv e-prints, astro-ph/1304.7778

Bernardi M., Meert A., Vikram V., Huertas-Company M., Mei S., Shankar F., Sheth R. K., 2012, ArXiv e-prints, astro-ph/1211.6122

Bernardi M., Roche N., Shankar F., Sheth R. K., 2011, MNRAS, 412, 684

Bernardi, M., Hyde, J. B., Sheth, R. K., Miller, C. J., Nichol, R. C., 2007, AJ, 133, 1741

Bernardi M., Sheth R. K., Annis J., Burles S., Eisenstein D. J., Finkbeiner D. P., Hogg D. W., Lupton R. H., et al., 2003, AJ, 125, 1849

Bertin E., Arnouts S., 1996, A&AS, 117, 393

Bertin E., Mellier Y., Radovich M., Missonnier G., Didelon P., Morin B., 2002, in Astronomical Society of the Pacific Conference Series, Vol. 281, Astronomical Data Analysis Software and Systems XI, Bohlender D. A., Durand D., Handley T. H., eds., p. 228

Binggeli B., Sandage A., Tarenghi M., 1984, AJ, 89, 64

Bland-Hawthorn J., Vlajić M., Freeman K. C., Draine B. T., 2005, ApJ, 629, 239

Blanton M. R., Kazin E., Muna D., Weaver B. A., Price-Whelan A., 2011, AJ, 142, 31

Bower R. G., Benson A. J., Malbon R., Helly J. C., Frenk C. S., Baugh C. M., Cole S., Lacey C. G., 2006, MNRAS, 370, 645

Boylan-Kolchin M., Springel V., White S. D. M., Jenkins A., Lemson G., 2009, MNRAS, 398, 1150

Bruzual G., Charlot S., 2003, MNRAS, 344, 1000

Bullock J. S., Johnston K. V., 2005, ApJ, 635, 931

Bullock J. S., Kravtsov A. V., Weinberg D. H., 2001, ApJ, 548, 33

Chabrier G., 2003, PASP, 115, 763

Chang, J., Macciò, A. V., & Kang, X. 2013, MNRAS, 431, 3533

Cole S., 1991, ApJ, 367, 45

Cole S., Lacey C., 1996, MNRAS, 281, 716

Cole S., Lacey C. G., Baugh C. M., Frenk C. S., 2000, MNRAS, 319, 168

Conselice C. J., 2006, MNRAS, 373, 1389

Cooper A. P., Cole S., Frenk C. S., White S. D. M., Helly J., Benson A. J., De Lucia G., Helmi A., et al., 2010, MNRAS, 406, 744

Cooper A. P., Martínez-Delgado D., Helly J., Frenk C., Cole S., Crawford K., Zibetti S., Carballo-Bello J. A., et al., 2011, ApJ, 743, L21

Conroy, C., Wechsler, R. H., & Kravtsov, A. V. 2006, ApJ, 647, 201

Courteau S., Widrow L. M., McDonald M., Guhathakurta P., Gilbert K. M., Zhu Y., Beaton R. L., Majewski S. R., 2011, ApJ, 739, 20

Cowie L. L., Gardner J. P., Hu E. M., Songaila A., Hodapp K.-W., Wainscoat R. J., 1994, ApJ, 434, 114

Crain R. A., Theuns T., Dalla Vecchia C., Eke V. R., Frenk C. S., Jenkins A., Kay S. T., Peacock J. A., et al., 2009, MNRAS, 399, 1773

Croft R. A. C., Di Matteo T., Springel V., Hernquist L., 2009, MNRAS, 400, 43

Croton D. J., Springel V., White S. D. M., De Lucia G., Frenk C. S., Gao L., Jenkins A., Kauffmann G., et al., 2006, MNRAS, 365, 11

Daddi E., Renzini A., Pirzkal N., Cimatti A., Malhotra S., Stiavelli M., Xu C., Pasquali A., et al., 2005, ApJ, 626, 680

de Jong R. S., 2008, MNRAS, 388, 1521

De Lucia G., Blaizot J., 2007, MNRAS, 375, 2

De Lucia G., Fontanot F., Wilman D., Monaco P., 2011, MNRAS, 414, 1439

De Lucia G., Springel V., White S. D. M., Croton D., Kauffmann G., 2006, MNRAS, 366, 499

Djorgovski S., Davis M., 1987, ApJ, 313, 59

Donzelli C. J., Muriel H., Madrid J. P., 2011, ApJS, 195, 15

Dutton A. A., van den Bosch F. C., Dekel A., Courteau S., 2007, ApJ, 654, 27

Eggen O. J., Lynden-Bell D., Sandage A. R., 1962, ApJ, 136, 748

Eke V. R., Frenk C. S., Baugh C. M., Cole S., Norberg P., Peacock J. A., Baldry I. K., Bland-Hawthorn J., et al., 2004, MNRAS, 355, 769

Faber S. M., Jackson R. E., 1976, ApJ, 204, 668

Fall, S. M., 1979, Nature, 281, 200

Font A. S., McCarthy I. G., Crain R. A., Theuns T., Schaye J., Wiersma R. P. C., Dalla Vecchia C., 2011, MNRAS, 416, 2802

Frenk C. S., White S. D. M., Efstathiou G., Davis M., 1985, Nature, 317, 595

Gallagher III J. S., Ostriker J. P., 1972, AJ, 77, 288

Gilbert K. M., Font A. S., Johnston K. V., Guhathakurta P., 2009, ApJ, 701, 776

Gnedin O. Y., Kravtsov A. V., Klypin A. A., Nagai D., 2004, ApJ, 616, 16

Gonzalez A. H., Zabludoff A. I., Zaritsky D., 2005, ApJ, 618, 195

González J. E., Lacey C. G., Baugh C. M., Frenk C. S., Benson A. J., 2009, MNRAS, 397, 1254

Graham A., Lauer T. R., Colless M., Postman M., 1996, ApJ, 465, 534

Graham A. W., 2011, ArXiv e-prints, astro-ph/1108.0997

Graham A. W., Driver S. P., Petrosian V., Conselice C. J., Bershady M. A., Crawford S. M., Goto T., 2005, AJ, 130, 1535

Graham, A. W., & Driver, S. P. 2005, PASA, 22, 118

Graham A. W., Guzmán R., 2003, AJ, 125, 2936

Guo Q., White S., Boylan-Kolchin M., De Lucia G., Kauffmann

G., Lemson G., Li C., Springel V., et al., 2011, MNRAS, 413, 101

Guo Q., White S., Li C., Boylan-Kolchin M., 2010, MNRAS, 404, 1111

Guo Q., White S. D. M., 2008, MNRAS, 384, 2

Guo Y., McIntosh D. H., Mo H. J., Katz N., van den Bosch F. C., Weinberg M., Weinmann S. M., Pasquali A., et al., 2009, MN-RAS, 398, 1129

Hernquist L., Spergel D. N., Heyl J. S., 1993, ApJ, 416, 415

Hilz, M., Naab, T., Ostriker, J. P., et al. 2012, MNRAS, 425, 3119

Hilz, M., Naab, T., & Ostriker, J. P. 2013, MNRAS, 429, 2924

Hopkins P. F., Hernquist L., Cox T. J., Dutta S. N., Rothberg B., 2008, ApJ, 679, 156

Hyde J. B., Bernardi M., 2009, MNRAS, 394, 1978

Ibata R. A., Gilmore G., Irwin M. J., 1995, MNRAS, 277, 781

Kauffmann G., 1996, MNRAS, 281, 487

Kauffmann G., Charlot S., 1998, MNRAS, 294, 705

Kauffmann G., Haehnelt M., 2000, MNRAS, 311, 576

Kauffmann G., Heckman T. M., White S. D. M., Charlot S., Tremonti C., Brinchmann J., Bruzual G., Peng E. W., et al., 2003a, MNRAS, 341, 33

Kauffmann G., Heckman T. M., White S. D. M., Charlot S., Tremonti C., Peng E. W., Seibert M., Brinkmann J., et al., 2003b, MNRAS, 341, 54

Kauffmann G., White S. D. M., Guiderdoni B., 1993, MNRAS, 264, 201

Kaviraj S., 2010, MNRAS, 406, 382

Koopmans, L. V. E., Bolton, A., Treu, T., et al. 2009, ApJ, 703, L51

Kormendy J., 1977, ApJ, 218, 333

Kormendy J., Fisher D. B., Cornell M. E., Bender R., 2009, ApJS, 182, 216

Krick J. E., Bernstein R. A., Pimbblet K. A., 2006, AJ, 131, 168

Laporte C. F. P., White S. D. M., Naab T., Ruszkowski M., Springel V., 2012, MNRAS, 424, 747

Laporte, C. F. P., White, S. D. M., Naab, T., Gao, L. 2013, ArXiv e-prints, astro-ph/1301.5319

Lauer T. R., Faber S. M., Richstone D., Gebhardt K., Tremaine S., Postman M., Dressler A., Aller M. C., et al., 2007, ApJ, 662, 808

Li C., White S. D. M., 2009, MNRAS, 398, 2177

Li Y.-S., White S. D. M., 2008, MNRAS, 384, 1459

Lin Y.-T., Mohr J. J., 2004, ApJ, 617, 879

LSST Science Collaborations, Abell P. A., Allison J., Anderson S. F., Andrew J. R., Angel J. R. P., Armus L., Arnett D., et al., 2009, ArXiv e-prints, astro-ph/0912.0201

Malin D. F., Carter D., 1983, ApJ, 274, 534

Martínez-Delgado D., Gabany R. J., Crawford K., Zibetti S., Majewski S. R., Rix H.-W., Fliri J., Carballo-Bello J. A., et al., 2010a, AJ, 140, 962

—, 2010b, AJ, 140, 962

Matthews T. A., Morgan W. W., Schmidt M., 1964, ApJ, 140, 35

McConnachie A. W., Irwin M. J., Ibata R. A., Dubinski J., Widrow L. M., Martin N. F., Côté P., Dotter A. L., et al., 2009, Nature, 461, 66

McMillan P. J., 2011, MNRAS, 414, 2446

Meert, A., Vikram, V., Bernardi, M., 2012, ArXiv e-prints, astro-ph/1211.6123

Meza A., Navarro J. F., Steinmetz M., Eke V. R., 2003, ApJ, 590, 619

Mihos J. C., Harding P., Feldmeier J., Morrison H., 2005, ApJ, 631, L41

Mitchell, P. D., Lacey, C. G., Baugh, C. M., Cole, S., 2013, ArXiv e-prints, astro-ph/1303.7228

Mosleh M., Williams R. J., Franx M., 2013, ArXiv e-prints, astro-ph/1302.6240

Moster B. P., Somerville R. S., Maulbetsch C., van den Bosch F. C., Macciò A. V., Naab T., Oser L., 2010, ApJ, 710, 903

Naab T., Johansson P. H., Ostriker J. P., 2009, ApJ, 699, L178

Naab T., Johansson P. H., Ostriker J. P., Efstathiou G., 2007, ApJ, 658, 710

Naab T., Khochfar S., Burkert A., 2006, ApJ, 636, L81

Napolitano, N. R., Pannella, M., Arnaboldi, M., et al., 2003, ApJ, 594, 172

Navarro, J. F., Frenk, C. S., & White, S. D. M. 1996, ApJ, 462, 563

Navarro J. F., Eke V. R., Frenk C. S., 1996, MNRAS, 283, L72

Niederste-Ostholt M., Belokurov V., Evans N. W., Peñarrubia J., 2010, ApJ, 712, 516

Oemler Jr. A., 1976, ApJ, 209, 693

Oser L., Ostriker J. P., Naab T., Johansson P. H., Burkert A., 2010, ApJ, 725, 2312

Parry O. H., Eke V. R., Frenk C. S., 2009, MNRAS, 396, 1972

Peñarrubia J., Navarro J. F., McConnachie A. W., 2008, ApJ, 673, 226

Peletier R. F., Davies R. L., Illingworth G. D., Davis L. E., Cawson M., 1990, AJ, 100, 1091

Pontzen, A., & Governato, F. 2012, MNRAS, 421, 3464

Purcell C. W., Bullock J. S., Zentner A. R., 2007, ApJ, 666, 20

Radburn-Smith D. J., de Jong R. S., Seth A. C., Bailin J., Bell E. F., Brown T. M., Bullock J. S., Courteau S., et al., 2011, ApJS, 195, 18

Reiprich T. H., Böhringer H., 2002, ApJ, 567, 716

Richardson J. C., Ferguson A. M. N., Mackey A. D., Irwin M. J., Chapman S. C., Huxor A., Ibata R. A., Lewis G. F., et al., 2009, MNRAS, 396, 1842

Robertson B., Bullock J. S., Cox T. J., Di Matteo T., Hernquist L., Springel V., Yoshida N., 2006, ApJ, 645, 986

Rozo E., Rykoff E. S., Evrard A., Becker M., McKay T., Wechsler R. H., Koester B. P., Hao J., et al., 2009, ApJ, 699, 768

Sales L. V., Navarro J. F., Theuns T., Schaye J., White S. D. M., Frenk C. S., Crain R. A., Dalla Vecchia C., 2012, MNRAS, 423, 1544

Salim S., Rich R. M., Charlot S., Brinchmann J., Johnson B. D., Schiminovich D., Seibert M., Mallery R., et al., 2007, ApJS, 173, 267

Schlegel D. J., Finkbeiner D. P., Davis M., 1998, ApJ, 500, 525

Schombert J. M., 1986, ApJS, 60, 603

—, 1988, ApJ, 328, 475

Schweizer F., 1980, ApJ, 237, 303

Schweizer F., Seitzer P., 1992, AJ, 104, 1039

Schweizer F., Seitzer P., Faber S. M., Burstein D., Dalle Ore C. M., Gonzalez J. J., 1990, ApJ, 364, L33

Searle L., Zinn R., 1978, ApJ, 225, 357

Seigar M. S., Graham A. W., Jerjen H., 2007, MNRAS, 378, 1575

Sèrsic J. L., 1968, Atlas de galaxias australes. Observatorio Astronomico, Cordoba

Shankar F., Marulli F., Bernardi M., Mei S., Meert A., Vikram V., 2013, MNRAS, 428, 109

Shen S., Mo H. J., White S. D. M., Blanton M. R., Kauffmann G., Voges W., Brinkmann J., Csabai I., 2003, MNRAS, 343, 978

Smith M. C., Ruchti G. R., Helmi A., Wyse R. F. G., Fulbright J. P., Freeman K. C., Navarro J. F., Seabroke G. M., et al., 2007, MNRAS, 379, 755

Somerville R. S., Primack J. R., 1999, MNRAS, 310, 1087

Springel, V., White, S. D. M., Jenkins, A., et al., 2005, Nature,

435, 629

Springel V., 2005, MNRAS, 364, 1105

Tal T., van Dokkum P. G., 2011, ApJ, 731, 89

Tal T., van Dokkum P. G., Nelan J., Bezanson R., 2009, AJ, 138, 1417

Thuan T. X., Romanishin W., 1981, ApJ, 248, 439

Toomre A., 1977, in Evolution of Galaxies and Stellar Populations, B. M. Tinsley & R. B. G. Larson D. Campbell, ed., pp. 401

Trujillo I., Förster Schreiber N. M., Rudnick G., Barden M., Franx M., Rix H.-W., Caldwell J. A. R., McIntosh D. H., et al., 2006, ApJ, 650, 18

Vale, A., & Ostriker, J. P. 2006, MNRAS, 371, 1173

van den Bosch F. C., Yang X., Mo H. J., 2003, MNRAS, 340, 771

van Dokkum P. G., Whitaker K. E., Brammer G., Franx M., Kriek M., Labbé I., Marchesini D., Quadri R., et al., 2010, ApJ, 709, 1018

Wang J., Navarro J. F., Frenk C. S., White S. D. M., Springel V., Jenkins A., Helmi A., Ludlow A., et al., 2011, MNRAS, 413, 1373

Wang W., White S. D. M., 2012, MNRAS, 424, 2574

Watkins L. L., Evans N. W., An J. H., 2010, MNRAS, 406, 264

White S. D. M., Frenk C. S., 1991, ApJ, 379, 52

White S. D. M., Rees M. J., 1978, MNRAS, 183, 341

Widrow L. M., 2000, ApJS, 131, 39

Zepf S. E., 1997, Nature, 390, 377

Zibetti S., White S. D. M., Brinkmann J., 2004, MNRAS, 347, 556

Zibetti S., White S. D. M., Schneider D. P., Brinkmann J., 2005, MNRAS, 358, 949

This paper has been typeset from a TEX/ LATEX file prepared by the author.